Chapter 4

Electroactive response of electrovector and ferroelectric ceramics

The ability of hydroxyapatite (HA) to convert readily into an electret under low polarizing field (≤ 1 kV/cm) makes it as an excellent substitute for electro-active prosthetic implants. The piezoelectric bioceramic sodium potassium niobate ($Na_xK_yNbO_3$, NKN, where $0 \leq x \leq 0.8$; $0.2 \leq y \leq 1$), with a unique combination of piezoelectric / electrical response, is also an excellent alternative to the electro-active prosthetic implants. In the present study, compacts of electrovector HA, ferroelectric $Na_{0.5}K_{0.5}NbO_3$ (NKN) and HA-25 vol % NKN were developed through spark plasma sintering route. The compacts of HA and NKN were then polarized at various polarizing fields of 30, 50 and 90 kV/cm, respectively, at 150˚C for 1h. While compact of HA-25 vol % NKN composite was polarized at 90 kV/cm. Thereafter, samples were depolarized at heating rates of 1, 5 and 10˚C/min, respectively. The study attempted to understand the behaviour of HA, polarized under very high E-field (~ 100 kV/cm) as compared with that of NKN which generally requires very high E-field to polarize (≥ 30 kV/cm). Further, in order to examine the effect of such a high E-field (90 kV/cm) on the bulk electrical properties, dielectric (ε) and ac conductivity behaviour of unpolarized and polarized (90 kV/cm) HA have been compared. Similar studies have been carried out for NKN and HA-25 vol % NKN composite as well. Thereafter, X-ray photoelectron spectroscopy (XPS) has also been performed for unpolarized and polarized (90 kV/cm) HA to analyse any alteration in surface chemistry due to polarization.

4.1. Material preparation

4.1.1. Materials

Electroactive bioceramics have been recognized as potential substrates for hard tissue replacement. This is due to the fact that bone is piezoelectric in nature and its piezoelectricity has been reported to play a crucial role in various bone metabolic activities as well as assists

in the healing of bone fractures and regeneration.[1,2,3] In this view, the electroactive bioceramics find their major role in bone implant applications.[2] In addition, such bioceramics can be developed into electro-active scaffolds which can mimic the bioelectrical nature of the living tissue and further facilitate the repair and growth/development of hard tissues such as bone and cartilage.[4] It has been reported that the developed piezoelectric scaffolds provide suitable electrical signals similar to the bioelectrical signals perceived in the extracellular matrix as well as in the bone remodelling and growth.[5] In bone, collagen is a major constituent which is responsible for the piezoelectric effect in bone.[2] In response to the internal forces /external forces, collagen develops electric charges/signals which transmit via ECM to the voltage gated channels of osteocyte cells.[4] The osteocyte cells are the main cellular systems responsible for the mechano-transduction property of the bone.[4] These osteocyte cells communicate with other bone cells such as osteoblasts and osteoclasts.[4] Therefore, the bioelectrical signals, generated in collagen, transmit to the intracellular compartment to the nucleus and thereafter, various cellular processes such as matrix production, cell growth and repair are induced.[4,6]

The surface electric potential on electroactive bioceramics enhances the osteobonding with bone tissue as well as induces favourable biological responses. In this backdrop, polarized hydroxyapatite (HA) has been an excellent choice as the induced surface charges via polarization has reported to significantly improve the crystallization of inorganic ions, *in-vitro* and *in-vivo*.[2,7,8] These surface charges enhance the protein adsorption on the material surface which affects the cell morphology, growth and proliferation.[2,7,8] In this perspective, a section has been dedicated in the literature review (chapter 2) which discusses the electroactive response of polarized HA and its biological response. Also, the structural, chemical and morphological similarity of HA with the mineral component of bone tissue makes it an excellent bioactive bone implant material. On the other hand, piezoelectric

bioceramics have also been suggested as an excellent alternative, as the surface charges, induced due to polarization increases the osteobonding.[9,10] In addition, piezoelctricity also assists in the healing of fractures.[11,12] It has also been proposed that the implanted piezoelectric scaffolds generate electrical charges / signals under biological loads which activate the voltage gated channels of bone cells resulting in increased intracellular Ca^{2+} concentration which enhance cell proliferation and thereby bone regeneration at the fractured site.[11,13,14,15] In this perspective, ferroelectric $Na_{0.5}K_{0.5}NbO_3$ (NKN) has been recognized among the excellent electroactive (piezoelectric strain coefficient: d_{33} ~ 161 pC/N, electromechanical coupling coefficient: k_p ~ 0.44 and mechanical quality factor: Q_m ~ 280) and biocompatible materials.[16,17] The development of prosthetic implant material with reasonable biocompatibility and electro-active response similar to that of bone is anticipated to be a potential alternative. In view of above, the development and consequences of polarized HA, NKN and HA-25 vol % NKN have been discussed elaborately in the subsequent sections.

4.1.2. Synthesis

Hydroxyapatite (HA) nanopowder was obtained from Sigma Aldrich, USA. The $Na_{0.5}K_{0.5}NbO_3$ (NKN) was synthesized using stoichiometric amounts of high purity (99.99%) grades of Na_2CO_3, Nb_2O_5 and K_2CO_3. The raw constituents were ball milled for 24 h in polyethylene jar using zirconia balls (5 mm dia) and acetone as milling media. After milling, the mixer was filtered and dried using rotary vacuum evaporator (N-1100, EYELA, Tokyo, Japan) and oven, respectively. The dried powder was calcined at 910˚C for 10 h with the heating rate of 5˚C/min. HA-25 vol % NKN was also prepared. In the process, the dried powders of HA with 25 vol % of NKN were balled milled for 16 h in acetone medium. The process allows the homogeneous mixing of both the constituents as well as facilitates the reduction in their particle sizes.

The spark plasma sintering (SPS, Model 515S, Fuji Electronic Industrial Co., Ltd, Saitama, Japan) route was adapted to sinter the powder compacts of HA, NKN and HA-25 vol % NKN composite. The samples were sintered at 950˚C for 5 min in vacuum [Fig. 4.1]. As depicted in Fig. 4.1, multi-stage sintering route was adapted. During the entire process, the constant pressure of 80 MPa was applied. The reduced atmosphere/vacuum sintering of NKN prevents the volatilization of alkali elements (Na and K), which provides superior densification as compared to conventional sintering techniques.[18] However, the reduced atmosphere sintering forms oxygen vacancies in the typical perovskite structure of NKN. Therefore, the developed compacts of HA, NKN and HA-25vol % NKN were annealed in air at 700˚C for 2 h to obtain the stoichiometric NKN as well as to remove the carbon contamination.

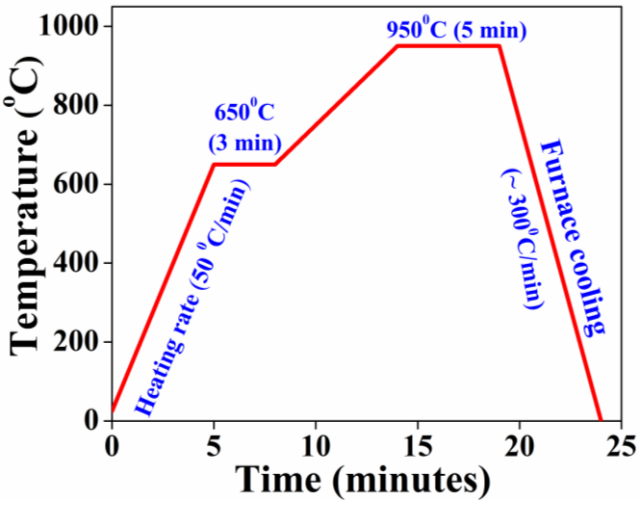

Fig. 4.1: Thermal sintering cycle, followed during spark plasma sintering of hydroxyapatite (HA), $Na_{0.5}K_{0.5}NbO_3$ (NKN) and HA-25 vol % NKN composite.

The SPS route is a rapid sintering technique which prevents diffusion, compositional fluctuations as well as formation of secondary phases.[19] SPS facilitates the development of high density (~ 99% of theoretical density) HA compacts at lower (100 - 200˚C) temperature than that of the conventional sintering techniques.[20,21] Sintering atmosphere affects the microstructure as well as electrical properties of HA. In addition, multi-stage SPS route has

been demonstrated to produce dense oxide and non-oxide ceramics which exhibits superior mechanical properties as compared to those prepared from single-stage route.[22] In perspective of HA- based composites, SPS route prevents abnormal grain growth, decomposition of HA phase as well as reaction between HA and reinforcement phase. Recently, it has been reported that HA, developed under different sintering atmospheres (water vapour and air), can be semi-permanently or permanently polarized due to the structural difference of their surfaces.[23] The permanently polarized HA has the ability to adsorb inorganic bioabsorbates which significantly improves its biomedical applications.[24] In addition, high temperature (> 1000˚C) conventional sintering induces OH^- defects in the crystal structure of HA. Low temperature sintering (< 1000˚C), however, can inhibit the formation of OH^- defects which plays the crucial factor in determining the electrical properties of HA. The present study utilizes the SPS route for consolidation of powder compacts, which has been reported to form OH^- defects at low temperature (850˚C) due to sintering in vacuum atmosphere.[25]

4.2. Phase evaluation and morphological characterization

X-ray diffraction (RAD-C, RIGAKU, Tokyo, Japan) analyses were performed to confirm the presence of different phases in the calcined powders as well as in SPSed compacts (2θ ~ 20 - 60° @ 0.02° /min). SPSed samples were mirror polished and the morphological analysis was performed by scanning electron microscopy (SEM, JSM-7001F, JEOL, Tokyo, Japan).

4.3. Dielectric measurement

For dielectric measurement, mirror polished samples were electroded with Ag-Pd paste and cured at 700˚C for 5 min in air. The dielectric response of the samples was recorded over a wide range of temperature (25˚C - 600˚C) and at 100 kHz of frequency using an impedance analyzer (4294A, Agilent Technologies Inc., Palo Alto, CA). Samples were heated at a heating rate of 3˚C/min. Further, the dielectric constant ($\varepsilon_r = \frac{Cd}{A\varepsilon_0}$, where, C, d and A are

capacitance, thickness and area of the samples, respectively and ε_0 is the permittivity of free space) and alternating current (σ_{ac}) conductivity (σ_{ac}= Gd/A; where G is the conductance; $G = \omega CD$; $\omega = 2\pi f$ and D are the angular frequency and dielectric loss, respectively) were evaluated.

4.4. Thermally stimulated depolarization current (TSDC) measurement

Thermally stimulated depolarization current (TSDC) is the study of temperature dependent relaxation in dielectrics and polymers.[26,27] The method employs, heating the sample till the polarizing temperature (T_p) and thereafter, applying a polarizing E-field (E_p) for a certain polarizing time (t_p). The sample is then cooled down to room temperature under sustained polarizing E-field (E_p). At room temperature, the polarizing field is removed and thereby, the sample is obtained in its polarized state. On reheating the polarized sample at a particular heating rate (β), the depolarization current is observed. The acquired TSDC spectra may consist of multiple relaxation phenomenons [Fig. 4.2]. These relaxations can be decomposed into individual relaxations using thermal sampling (TS) method.[28,29,30,31,32,33,34] Each individual relaxation is characterized by its activation energy (E_a).[34]

The TSDC is the depolarized current density [$J(t)$] which can be defined as the rate of discharge of frozen polarization [$P(t)$] with time,[35]

$$-\frac{dP(t)}{dt} = J(t) \tag{4.1}$$

Assuming that the $P(t)$ decays with a single temperature dependent relaxation time [$\tau(T)$], then accordingly,[36]

$$\frac{dP(t)}{dt} = -\frac{P(t)}{\tau(T)} \tag{4.2}$$

Integrating eq. (4.2), one can obtain,

$$P(t) = P_o e^{\left[-\int_{t_i}^{t_f} \frac{1}{\tau(T)} dt\right]} \tag{4.3}$$

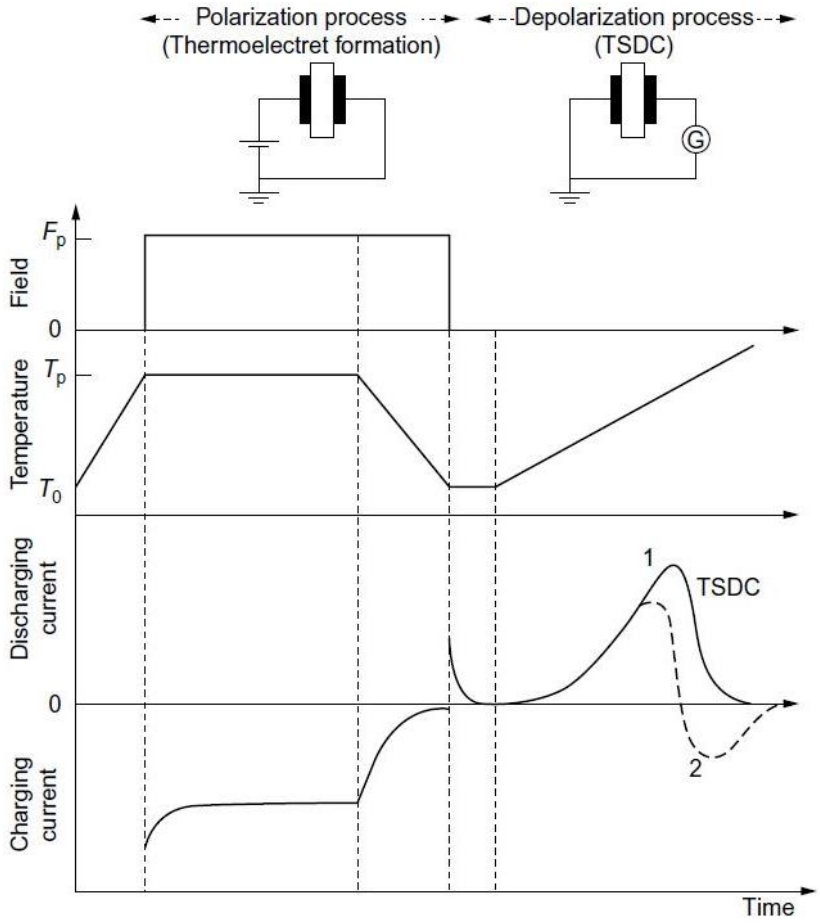

Fig. 4.2: Schematic illustration of the methodology, utilized for the thermally stimulated depolarized current measurement (TSDC).[37] (Reproduced with permission from Springer Nature)

Where, P_o is the initial polarization established during poling, t_i and t_f are the initial and final time durations of measurement of depolarization current. Considering eqs. (4.1) and (4.2), relaxation time $\tau(T)$ can also be expressed as,

$$\tau(T) = \frac{P(t)}{J(t)} \tag{4.4}$$

Where, $P(t) = \int_{t_i}^{t_f} J(t)dt$, therefore, eq.(4.4) can be rewritten as,

$$\tau(T) = \frac{\int_{t_i}^{t_f} J(t)dt}{J(t)} \tag{4.5}$$

Eq. (4.5) can also be expressed as a function of temperature (*T)* as,

$$\tau(T) = \frac{1}{\beta J(T)} \int_{T_i}^{T_f} J(T)dT \tag{4.6}$$

Where, T_i and T_f are the initial and final temperatures of measurement, corresponding to initial and final time of measurement (t_i, t_f) and $\beta = dT/dt$ is the heating rate with which the TSDC is measured. Using eqs. (4.1), (4.2) and (4.3), current density can be expressed as,

$$J(T) = \frac{P_o}{\tau(T)} e^{-\frac{1}{\beta}\int_{T_i}^{T_f} \frac{1}{\tau(T)}dT} \tag{4.7}$$

For the measurement of the TSDC, it is generally assumed that the relaxation time [$\tau(T)$] of the relaxation processes in dielectrics follows Arrhenius law. Therefore, the temperature dependent relaxation time is expressed as, $\tau(T) = \tau_o e^{\frac{E_a}{k_B T}}$, where, τ_o is the pre-exponential factor and E_a and k_B are activation energy for the relaxation of the dipoles and Boltzmann's constant, respectively.[26] It is a Debye relaxation rate which assumes that the decay of the polarization with time follow first-order kinetics. Therefore, eq. (4.7) can also be expressed as,

$$J(T) = \frac{P_o}{\tau_o} e^{-\frac{E_a}{k_B T}} e^{\left[-\frac{1}{\beta\tau_o}\int_{T_i}^{T_f} e^{\left(-\frac{E_a}{k_B T}\right)}dT\right]} \tag{4.8}$$

Eq. (4.8) is also called Bucci-Feischi theory.[26] It consists of two exponentials, the first exponential is dominant at lower temperatures, depicting the increase in the TSDC (increase in the relaxation of dipolar polarization) with temperature. The second exponential dominates at higher temperatures that gradually counter the increase in TSDC (exhaustion of induced polarization progresses) until a maxima is reached. The TSDC spectrum is, therefore, symmetric with respect to temperature. According to Bucci-Feischi theory, the spectrum of TSDC represents the current due to the relaxation of the dipolar polarization. Therefore, the associated activation energy (E_a) also depicts the relaxation of dipolar polarization. However, the activation energy can also be associated with space charge conduction due to space charge polarization with the assumption that the mobility of all the polarized charges is same.[38,39] Therefore, the initial polarization (P_o) consists of dipolar as well as space charge polarization.[38] Considering the fact that polarization consists of only dipolar polarization (P_{DP}), the initial polarization P_o attained after poling, can be expressed as,

$$P_{DP}(P_o) = \frac{Nm^2 E_p}{3k_B T_P} \tag{4.9}$$

Eq. (4.9) is known as the Langevin-Debye equation,[40] where the parameters N, and m denotes the density of the dipoles per unit volume and electric dipole moment, respectively. The eq. (4.9) suggests that the dipolar polarization is a function of polarizing field (E_p) which are linearly proportional to each other. If polarization is inclusive of space charge polarization (P_{SC}), then it is expressed as,[41]

$$P_{SC} = 2qvNqt_p e^{\left[-\frac{E_a}{k_B T}\right]} \sinh\left(\frac{qaE_p}{2k_B T_p}\right) \tag{4.10}$$

In this equation, q is the ionic charge, N is the mobile charges per unit volume, a is the potential barrier for the ion to escape from the trap or it is the jump length and v is the escape

frequency of the ion from the trap. Eq. (4.10) signifies the exponential relationship between space charge polarization and the polarizing E-field (E_p). Therefore, TSDC consists of depolarization current due to dipolar as well as space charge polarization. Under the assumption that these currents are linearly dependent on each other, the TSDC can be expressed as,

$$I_{TSDC} = I_{DP} + I_{SC} + EC_O \exp(U / k_B T) \tag{4.11}$$

I_{DP}, I_{SC} are the currents due to dipolar as well as space charge polarization. The third expression is the stray current due to Ohmic conductivity.[38] The ohmic conductivity and thermo-electromotive force E are usually small at low temperature but rises exponentially with increase in temperature. Determining the polarization parameters such as P_{DP}, P_{SC}, τ_o, E_a and the stray current, the TSDC spectrum can be reproduced. Eq. (4.8) can also be expressed as,

$$\frac{E_a}{k_B T} + \ln \tau_o = \ln\left[\frac{1}{\beta}\int_{T_i}^{T_f} J(T)dT\right] - \ln J(T) \tag{4.12}$$

As mentioned before, the obtained TSDC spectrum consists of multiple relaxations, therefore, to evaluate the associated activation energy with each relaxation, the spectrum can be deconvoluted. Each deconvoluted peak would consist of peak temperature (T_m) at which maximum current is observed. Therefore, activation energy can be evaluated from the slope of linear curve between $ln\ \tau$ v/s $1/k_BT$. In this method, the area under each deconvoluted spectrum is utilized to evaluate the associated activation energy.[42] This method is known as the area method or the initial rise method. In the present study, the area method was applied to evaluate the activation energy of the TSDC spectra of HA.

The other method, generally called the peak temperature method, can also be utilized to evaluate the associated activation energies of the deconvoluted peaks.[35,36,43] It can, therefore,

be described as the temperature, at which the peak current density is observed, can be evaluated from the eq. (4.8), by $dJ(T)/dT = 0$, one can obtain,

$$\frac{T_m^{\,2}}{\beta} = \frac{E_a \tau_o}{k} e^{\frac{E_a}{kT_m}} \Rightarrow T_m = \left(\frac{E_a \beta \tau_o}{k} e^{\frac{E_a}{kT_m}} \right)^{\frac{1}{2}} \tag{4.13}$$

Using eq. (4.13), activation energy can be evaluated from the slope of the linear curve plotted between $ln\ (T_m^2/\beta)$ *v/s* $(1/T_m)$. Eq. 4.13 also suggests the influence of heating rate (β), τ_o, and E_a on the position of peak temperature (T_m) in the TSDC spectra. From eq. 4.13, it can be suggested that as the heating rate increases, the relaxation in initial polarization does not happen instantaneously, that is why, the relaxation peaks are shifted to higher temperature in the TSDC spectra.[37] Therefore, to increase the resolving power of TSDC i.e. to obtain the maximum relaxations, slow heating can be utilized. However, in the end heating rate might influence the TSDC, but overall spectra depends on τ_o and E_a.[37] The charge stored (Q_P) in the sample during polarization can be evaluated from the TSDC spectra as,[43]

$$Q_P = \frac{1}{\beta} \int_{T_i}^{T_f} J(T) dT \tag{4.14}$$

Spark plasma sintered compacts of HA and NKN were polarized at various polarizing E-field (E_p) intensities of 30, 50 and 90 kV/cm at polarizing temperature (T_p) of 150˚C for 1 h in a silicon oil bath. SPSed compact of HA-25 vol % NKN composite was polarized at 90 kV/cm. The compacts were cooled down to room temperature under the constant exposure of polarizing E-field. The polarized samples were kept at room temperature for a day to release the surface/stray charges. Thereafter, the polarized samples were heated at various heating rates of 1˚, 5˚ and 10˚C/min, respectively up to 500˚C and consequently, thermally stimulated

depolarization current (TSDC) measurements were performed using a picoammeter (Model 6487, KEITHLEY, Solon, OH).

4.5. X-ray photoelectron spectroscopy (XPS) analyses

The polarization at such a high field (~ 100 kV/cm) can raise the concern of alteration in the surface chemistry of HA. To address this issue, the surface sensitive analytical tool, X-ray photoelectron spectroscopy (XPS) has been used to study the surface characteristics of the unpolarized and polarized surfaces of SPSed HA. XPS becomes important as the surface chemistry plays a crucial role during interfacial interaction of implant with the host tissue. Also, such treated samples may likely to have different compositions near the surface and in the bulk, and therefore, bulk characterization often leads to misinterpretation of structure/function relationships during interfacial interaction.

4.6. Results and discussion

4.6.1. Phase analyses and microstructure

The densification of SPSed HA, NKN and HA-25 vol % NKN samples was about 99% which is reasonably higher than that of conventionally sintered samples.[44] Fig. 4.3 [(a) and (b)] represents the X-ray diffraction (XRD) patterns of calcined as well as SPSed HA and NKN. The XRD pattern of sintered HA [Fig. 4.3(a)] reveals the presence of pure hexagonal phase (JCPDS no. 09-0432) without any appearance of secondary phases. The XRD pattern of sintered NKN [Fig. 4.3(b)] reveals the formation of pure orthorhombic perovskite phase which has been indexed using ICSD file no. 247571.

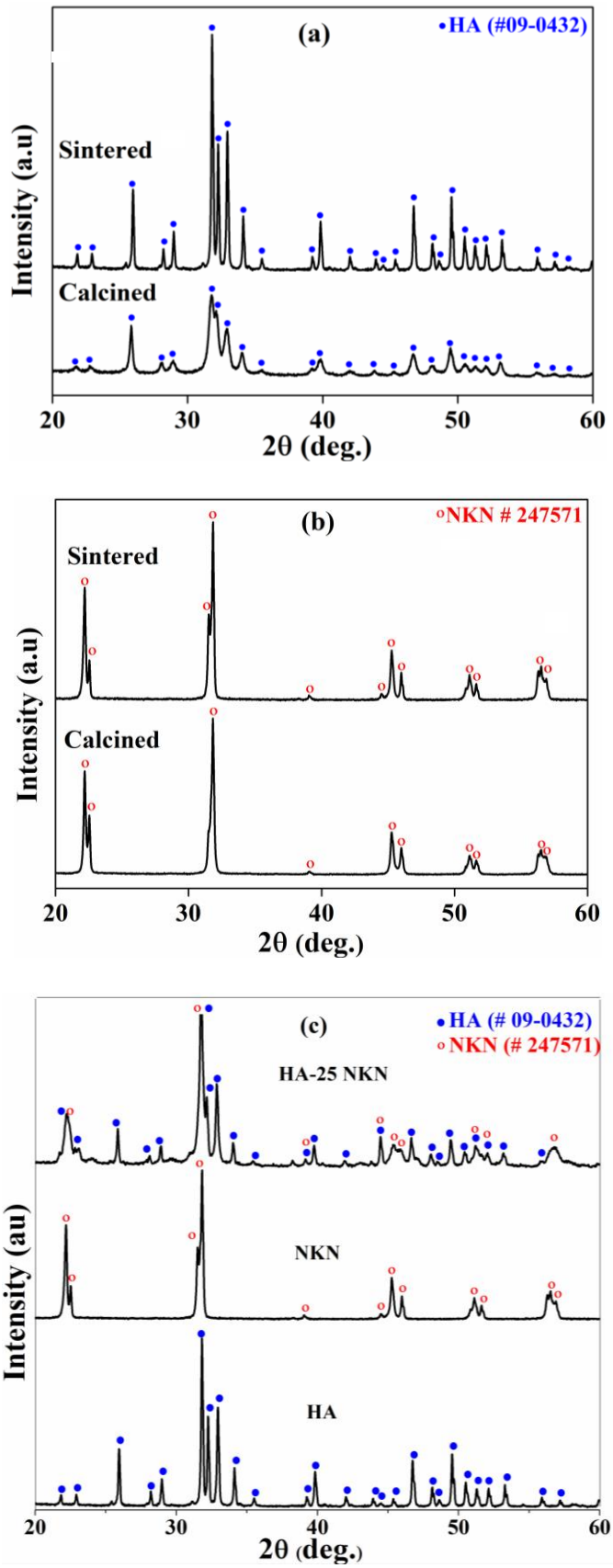

Fig. 4.3: X-ray diffraction spectra for calcined as well as sintered (a) HA and (b) $Na_{0.5}K_{0.5}NbO_3$ (NKN), and (c) HA-25 vol % NKN composite.

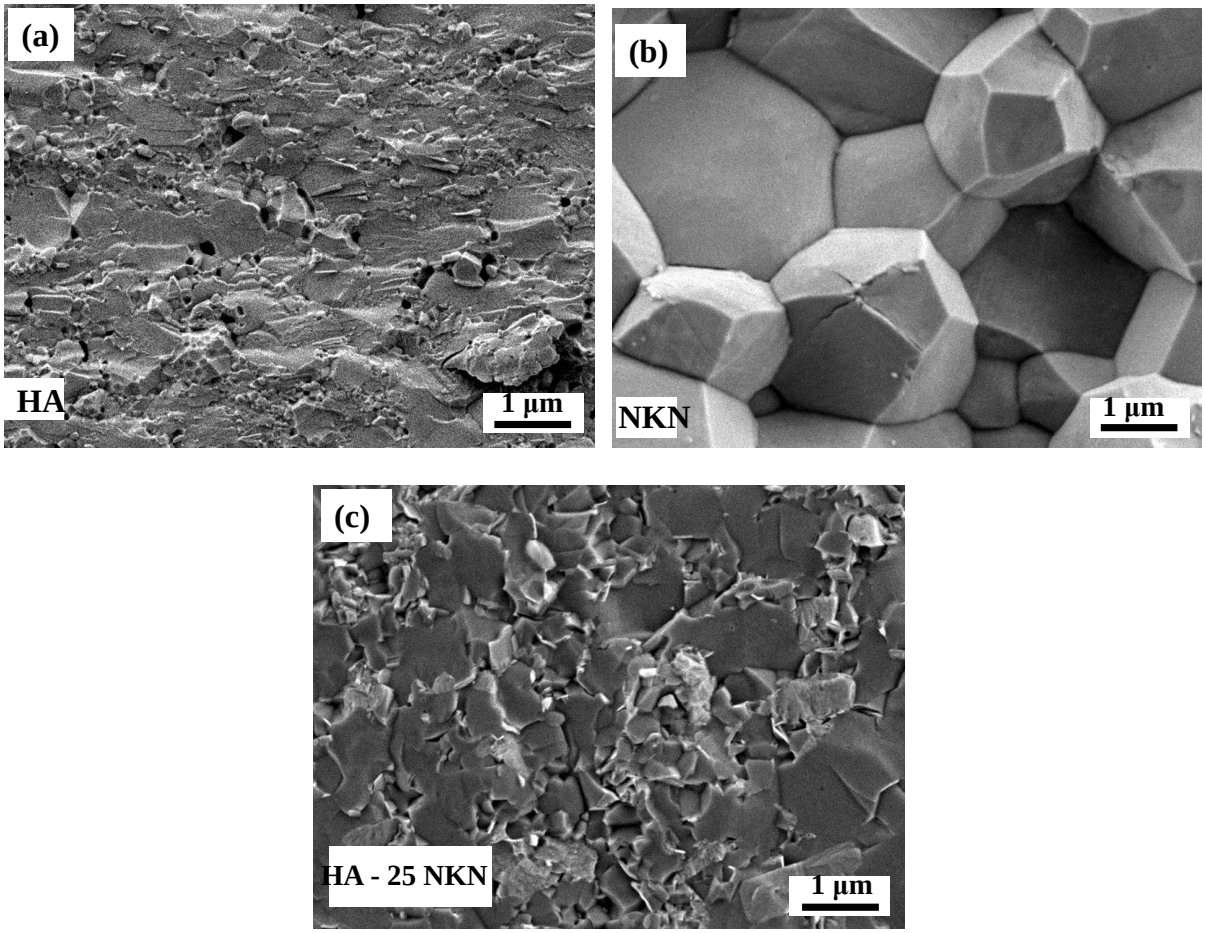

Fig. 4.4: Scanning Electron Microscopic images of fractures surfaces of SPSed (a) HA, (b) NKN and (c) HA-25 vol % NKN composite.

The intensities of the peaks, corresponding to pure HA and NKN phases are observed to be higher for the sintered samples than the calcined samples. Fig. 4.3(c) represents the XRD pattern of SPSed HA-25 vol % NKN composite. The pattern depicts the presence of both HA and the reinforcement phase i.e., NKN in the composite without any sign of dissociation or reaction between the constituent phases. Figs. 4.4(a), 4.4(b) and 4.4(c) represent the microstructure of fractured surfaces of HA, NKN and HA-25 NKN composite, respectively. The dense microstructure is evident from all the images. Also, the brittle mode of fracture is observed as the dominant mode of fracture.

4.6.2. TSDC characteristics of HA

Fig. 4.5 represents the variation of thermally stimulated depolarization current of HA with the temperature at heating rates of 1, 5 and 10˚C/min, respectively. The samples were polarized at 30 kV/cm [Fig. 4.5(a)], 50 kV/cm [Fig. 4.5(b)] and 90 kV/cm [Fig. 4.5(c)], respectively. The TSDC spectrum is observed to depend on external polarizing E-field (E_p) as well as the heating rate (β) (for depolarization). For depolarization at a heating rate of 1˚C/min, the current density peak (J_{max}) appears to shift towards higher temperatures (> 500˚C) with the increase in E_p from 30 to 90 kV/cm. Similar depolarization behaviour is observed at a heating rate of 5˚C/min. However, few peaks are observed at ~ 450˚C during the cooling phase, which represents that the samples are not completely depolarized up to 500˚C. For the depolarization at a heating rate of 10˚C/min, peaks are observed in the lower temperature range (100˚C - 300˚C) for E_p of 30 and 90 kV/cm [Figs. 4.5(a) and (c)]. From the TSDC spectra, the charge (Q_p), stored in HA can be evaluated using eq. (4.14).[43]

The maximum current density (J_{max}) and charge (Q_p), stored by polarization at various polarizing fields (30 - 90 kV/cm) are provided in table 4.1. It is observed that with the increase in the intensity of the polarizing field from 30 to 90 kV/cm, the peak current density (J_{max}) increases for depolarization at a heating rate of 1˚C/min. Also, for depolarization at 1˚C/min, the amount of charge increases significantly with the increase in polarizing E-field as compared with depolarization at heating rates of 5 and 10˚C/min. The significant increase in charge density (Q_p) with polarizing field (E_p) is only observed for depolarization at 1˚C/min. This can be due to the fact that with slow heating rate (β), maximum number of relaxations in dielectric has taken place while with increase in heating rate (β), several relaxations do not happen and therefore, a dielectric responds slowly.[37]

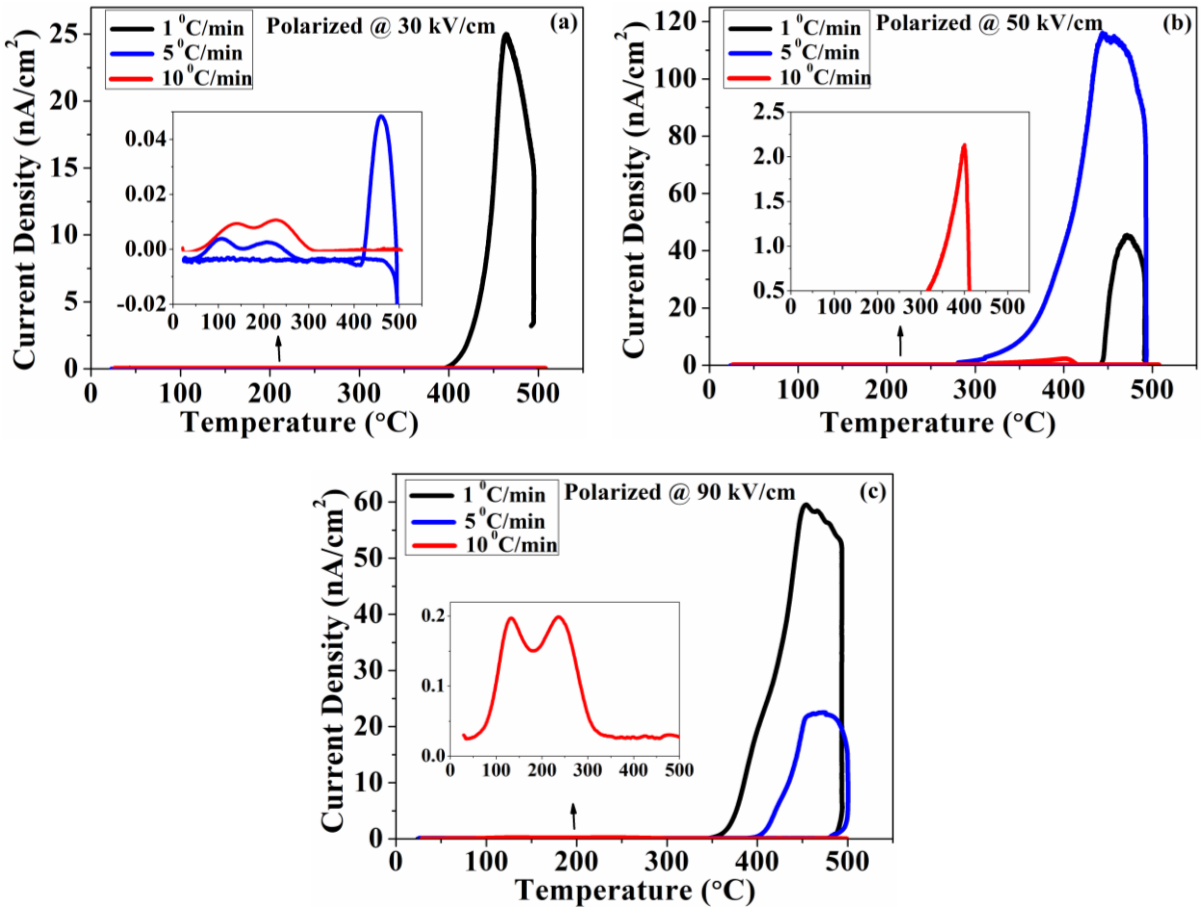

Fig. 4.5: Thermally stimulated depolarization current (TSDC) spectra for HA, polarized at E-field strength of a) 30 kV/cm, b) 50 kV/cm and c) 90 kV/cm, respectively. The depolarization current was measured, while heating the polarized samples at heating rates of 1, 5 and 10˚C/min, respectively.

As already mentioned, the TSDC spectra [Fig. 4.5 (a) & (c)] consists of multiple relaxation phenomenon, therefore using area method, activation energy can be evaluated from the slope of the linear curve plotted between $ln\ \tau$ v/s $1/k_BT$ [Fig. 4.6 (a)-(i), (a)-(ii), (b)-(i), (b)-(ii)].

Table 4.1: Depolarization response of HA as a function of polarizing field and heating rate.

Polarizing E-field (E_p) (kV/cm)	Peak Temperature(T_{max}) (˚C)	J_{max} (nA/cm^2)	Q_P	Heating rate (β)(˚C/min)
30 kV/cm	464	24.8	1.12 µC/cm^2	1
	460	0.04	0.175 nC/cm^2	5
	230	0.12	0.214 nC/cm^2	10
50 kV/cm	472	45.04	1.65 µC/cm^2	1
	445	115.3	1.15 µC/cm^2	5
	400	2.12	9.49 nC/cm^2	10
90 kV/cm	453	59.47	2.27 µC/cm^2	1
	476	22.4	0.15 µC/cm^2	5
	236	0.198	4.1 nC/cm^2	10

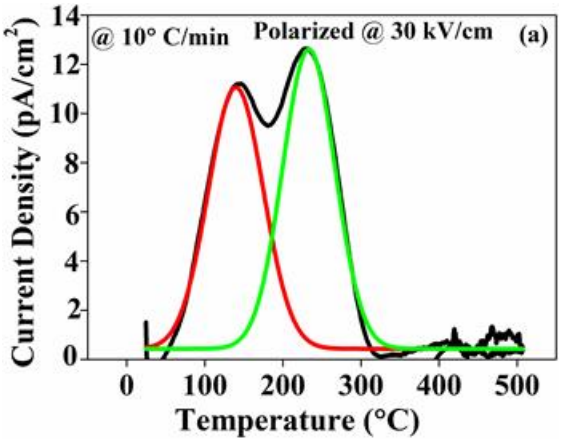

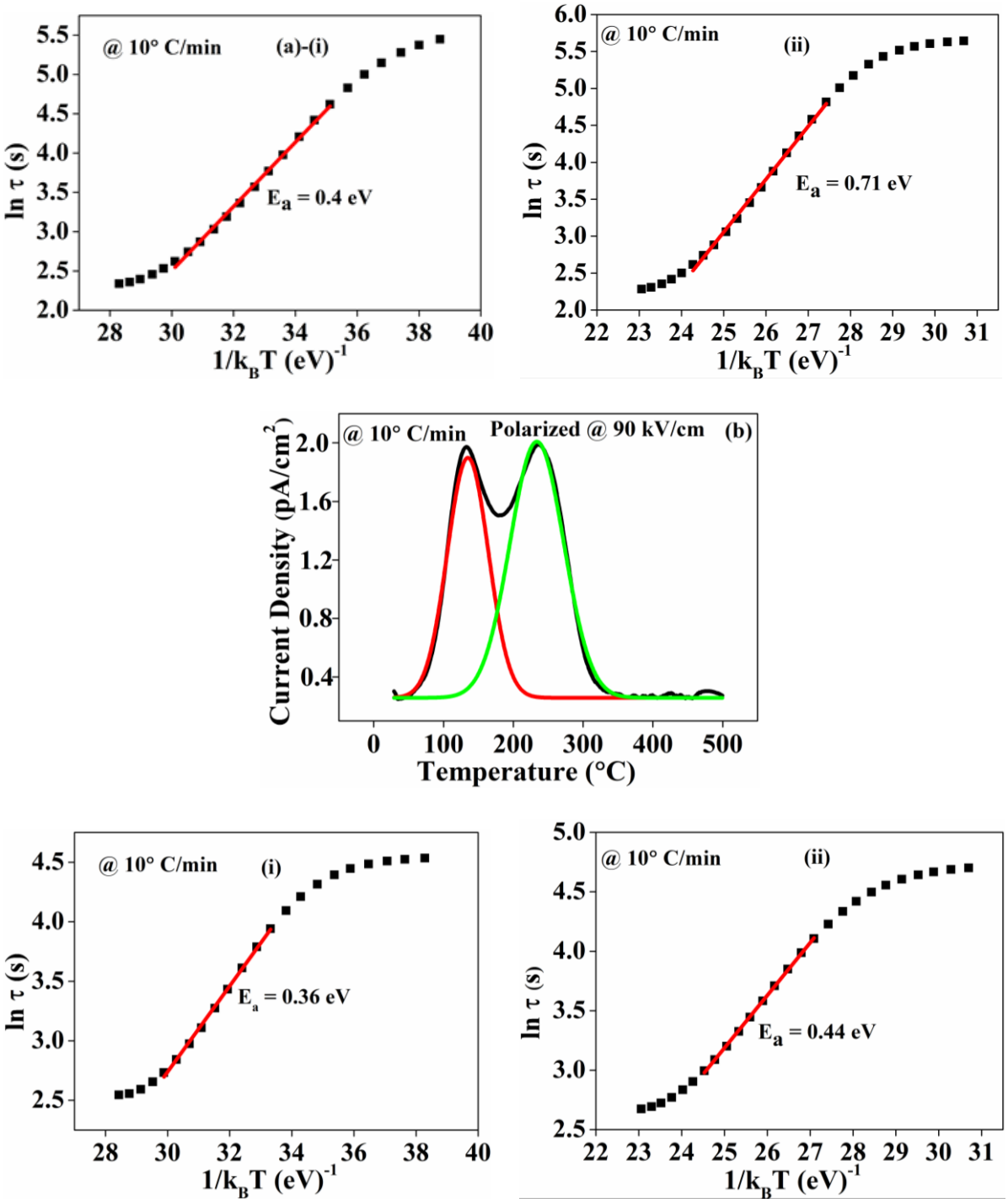

Fig. 4.6.: Deconvoluted TSDC spectra of HA, depolarized at the heating rate of 10˚C/min after polarization at a) 30 kV/cm and b) 90 kV/cm. The respective Arrhenius plots (a)-(i), (a)-(ii), (b)-(i) and (b)-(ii) depicting the activation energies, obtained from deconvoluted spectra.

4.6.2.1. Mechanism of polarization and depolarization in HA

The polarization of HA is more sensitive towards polarizing temperature (T_p) rather than the polarizing field (E_p).[45] This is because the mobility of OH^- ions in HA as well as the protonic conductivity is highly dependent on polarizing temperature.[45] However, in the present study, all the SPSed samples were polarized at low polarizing temperature (T_p = 150˚C) and high electric field (30 - 90 kV/cm). Apart from temperature, polarizing electric field also affects the mobility of ionic species [O^{2-}, protons (H^+) and OH^- ions] as well as the orientations of OH^- dipoles in the HA lattice. It can be seen in the Figs. 4.5 (a) and (b), that the steepness of the curve increases for depolarization at 1˚C/min for E_p of upto 50 kV/cm. Dual peaks for the depolarization at a heating rate of 10˚C/min in the lower temperature range (100˚C - 300˚C) represents the relaxation phenomenon [Figs. 4.5 (a) and (c)]. After deconvoluting the peaks, the corresponding activation energies were observed to lie in the range of 0.4 - 0.7 eV [Fig. 4.6]. Further, it has been suggested through simulation studies that dominant polarization in HA mostly occurs via three main processes i.e., reorientation of the OH^- ions, proton hopping/migration through oxide (O^{2-}) ions / proton vacancy sites and hopping of OH^- vacancies, all of which occur along the columnar OH^- channels of the lattice.[46] It is also reported that the TSDC spectra of polycrystalline HA consist of four polarization states with each state having different activation energies.[45] The activation energy for the first polarization state is ~ 0.4 eV, which is associated with the orientational polarization due to absorbed water.[45] Whereas, the activation energy of the second and third polarization state is ~ 0.6 eV which is due to the three dimensional proton (H^+) migration / conduction via PO_4^{3-} tetrahedra and OH^- ions along columnar c-axis.[45] In another report, it has been suggested that the activation energy in the range of 0.67 - 0.86 eV is associated with proton (H^+) conduction along columnar c-axis.[38] The low activation energy values [Fig. 4.6 (a)-(i), (a)-(ii), (b)-(i), (b)-(ii)] correspond to short range proton (H^+) conduction through columnar c-axis. It can

also be suggested here that the relaxation peaks [Fig. 4.5 (a) and (c)] for depolarization at 10˚C/min in lower temperature range (100˚C - 300˚C) are associated with the orientational polarization due to water of hydration. In addition, the lower current density, for the heating rate of 10˚C/min, is probably due to the incomplete depolarization within our measuring temperature range [Fig. 4.5 (a) and (c)]. The activation energies, associated with the heating rates of 1 and 5˚C/min, could not be evaluated because in the former case, the depolarization current density peaks appear to shift towards higher temperature (> 500˚C) with the polarizing field (E_p) and in the latter case, depolarization current density peaks are observed in the cooling phase.

In the context of above results, detailed mechanisms of polarization and depolarization occurring in HA is presented herewith.

The polarization of HA takes place at elevated temperature under intense polarizing field.[43] Fig. 4.7 (a) illustrates the orientation of the OH^- along c-axis in the hexagonal lattice. As mentioned above, the protons (H^+) along c-axis become highly unstable as temperature increases above 200˚C.[47] Therefore, under strong polarizing field, movement of the protons can be controlled which can further establish the polarization of HA. It has been suggested through TSC (Thermally stimulated current) measurement of HA, that the polarization is based on the reorientation of the OH^- dipoles.[48,49,50] Fig. 4.7 (b) subsequently represents the reorientation of the OH^- dipoles which takes place at higher temperatures. The model is called the proton rotation model.

Accordingly, at high temperature, when the bond between protons (H^+) and oxygen (O^{2-}) is unstable, the protons (H^+), present on the O^{2-}, rotate and align under sustained E-field. The alignment of OH^- get freezes up in low temperature region. When reheated, the alignment gets disturbed and simultaneously relaxes via rotation of the protons (H^+). The relaxation of the proton rotation depicts phase transition from monoclinic to hexagonal at almost

211˚C.[51,52,53] The activation energy of the relaxation of the rotation, evaluated through the thermal sampling method is found to vary between 0.016 to 0.630 eV.[48,49] Overall, the model suggests that the polarization and depolarization in HA occurs via reorientation ability of the OH^- ions/dipoles under the applied polarizing field.

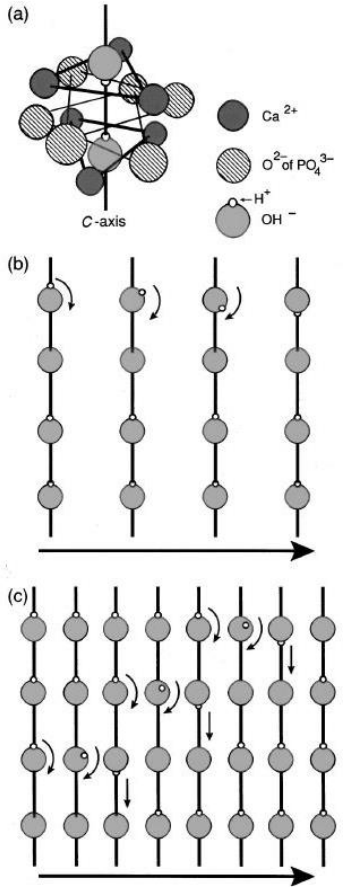

Fig. 4.7: Schematic representing the (a) arrangement of hydroxide (OH^-) ion in the hexagonal unit cell, (b) the proton rotation model indicating the mechanism of polarization and depolarization from left to right and (c) the migration of protons by rotation around the O^{2-} ions to the adjacent proton vacancy site.[43] (Reproduced with permission from AIP publishing)

However, due to the mobility of the protons (H^+) of the hydroxyl (OH^-) group in OH^- columns, proton rotation model did not suffice to explain the polarization mechanisms in HA.[47] In addition, it has been reported that in yttrium-substituted calcium oxyhydroxyapatite

$(Ca_{10-x}Y_x)(PO_4)_6((OH)_{2-2x}O_x\square_x)$; □ = vacancies) having defects of OH^- ions and protons (H^+), the conduction of protons (H^+) and oxide (O^{2-}) ions takes place simultaneously at elevated temperature (≥ 700˚C).[54] Also, in fluorine substituted HA, conduction through OH^- diffusion via OH^- vacancies is observed with the activation energy of ~ 2.4 eV.[55,56] As significant polarization in HA takes place at higher temperature, the role of conducting species such as H^+, OH^- and O^{2-} ions during polarization and depolarization is evident.[47,57] As shown in Fig. 4.7 (c), one such polarization mechanism is based on the proton (H^+) vacancy on O^{2-} ion at OH^- site. Consequently, the proton (H^+), present on the O^{2-} ions, rotates and thereafter, migrates to the neighbouring proton-vacancy site (O^{2-}). Therefore, in the process, the long range migration of protons occurs along c-axis channels. Another possible conduction path of proton migration would be via PO_4^{3-} tetrahedra due to its relatively shorter distance than the adjacent OH^- site. The associated activation energy for this type of proton migration has been evaluated to be in the range of 0.7 - 0.9 eV.[43]

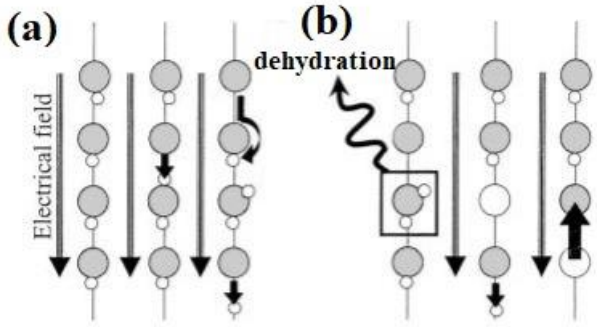

Fig. 4.8: Schematic illustration of (a) proton migration along c-axis in the applied field direction from left to right and (b) the process of dehydration and consequently, the diffusion of oxide (O^{2-}) ions from upper to lower sites after dehydration and thereafter, lower to upper sites along c-axis.[58] (Reproduced with permission from John Wiley and sons)

The TSDC parameter such as, polarizing temperature significantly influences the stored charge in HA.[45,58] Therefore, it has been suggested that the polarization and depolarization in HA take place through ionic diffusion.[58] Also, as polarization temperature increases, the associated activation energy increases, depicting that the different mechanisms of polarization and depolarization contributes at different temperatures. It has been reported that the activation energy of almost 1 eV is associated with the proton migration through HA lattice for the polarization temperature of almost 400˚C.[56,58] The migration of protons through the rotation around OH^- ions requires the proton vacancy in the adjacent OH^- site but the hypothesis of occurrence of this type of vacancy is implausible.[56] It is due to the fact that the protons (H^+) are loosely associated with O^{2-} ions in the OH^- group at elevated temperature and therefore, get dissociated easily to exhibit proton conduction through the HA lattice.[47] As the temperature of polarization (T_p) increases above 400˚C, the stored charge density (Q) in HA increases (15 μC cm^{-2} to 1.2 mC cm^{-2}) with the increase in associated activation energy (> 1 eV).[58] At such high temperature, the partial dehydration of HA takes place, leaving the vacancies at lattice OH^- sites and therefore, the ions such as O^{2-} and OH^- are proposed to conduct.[58] Simulation results suggest that the O^{2-} ions have comparatively larger mobility than the OH^- ions.[55] In addition, it has been demonstrated that the diffusion of O^{2-} ions occurs with the associated activation energy of almost 2 eV.[55] Overall, it can be suggested that with lower polarization temperature (≤ 400˚C), the polarization and depolarization is mediated through proton conduction, dissociated from the OH^- ions.[56] At higher values of polarizing temperature (≥ 400˚C), diffusion of O^{2-} ions through the HA lattice HA takes place along with partial dehydration [Fig. 4.8].[58,59] The study suggested that the stored charge density in HA electrets vary between 0.1 μC cm^{-2} and 1.2 mC cm^{-2}.[58] In addition, it significantly depends on the polarization temperature and slightly on polarizing field.[58]

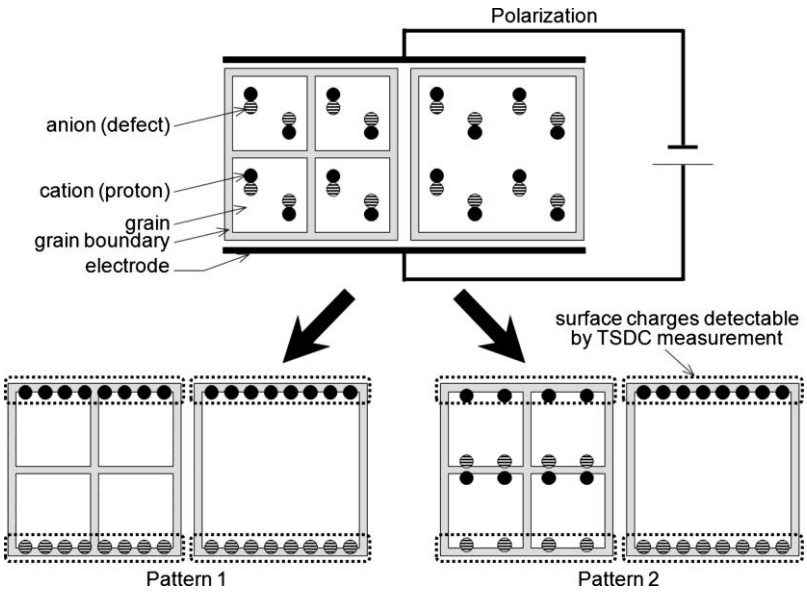

Fig. 4.9: Schematic representation of the polarization process occurring in the polycrystalline HA with different grain sizes and similar carrier density. Pattern 1 depicts the accumulated charge after polarization without the hindrance of the grain boundaries and Pattern 2 reveals the influence of grain boundaries on the accumulated charge, after polarization.[45] (Reproduced with permission from AIP publishing)

For the case of polycrystalline HA, as the polarizing temperature increases (250˚C to 500˚C), the peak of the depolarization current (TSDC) shifts to higher temperatures (250˚C to 620˚C).[45] In addition, the stored charge density in HA also increases (0.5 to 45 μC cm^{-2}).[45] The average grain size in polycrystalline HA also influences the stored charge with negligible effect on the TSDC characteristics.[45] As the average grain size increases (2 to 11 μm), the stored charge density increases from 15 to 60 μC cm^{-2}.[45] The variation in poling condition such as, polarizing time as well as polarizing field along with the variation of the microstructure of the polycrystalline HA resulted in the TSDC spectrum which theoretically consists of four polarization states.[45] The first polarization state with activation energy of 0.4 eV is associated with the orientational polarization of the adsorbed water.[45] Second and third polarization state is due to the hopping of the protons (H^+) via PO_4^{3-} tetrahedra as well as OH^- ions sites in the grains and the associated activation energy is almost 0.6 eV.[45] Fourth

polarization state is suggested to be associated with the migration of protons within the grain boundaries with the activation energy of almost 1 eV.[45] It should be emphasized that the activation energy is not influenced by the grain size.[45]

It is well known that the grain boundaries are regions of high impedance for ionic conduction. Therefore, polarization charges are greatly influenced by their sizes.[45] Fig. 4.9 schematically represents the polarization in the polycrystalline HA having different grain sizes with the assumption of equal carrier densities (H^+). The patterns one and two illustrate different polarization charges which are accumulated after poling. The pattern one suggests that if the proton migration is free from the influence of grain boundaries, similar charges will be accumulated after poling the polycrystalline HA compacts, irrespective of grain sizes. While pattern two reveals the effectiveness of the grain boundaries which obstruct the proton conduction and therefore, the charge accumulated, after poling, is different for different grain sizes.[45]

In all the above mentioned polarization mechanisms, proton conductivity in HA has played significant role. In addition, the polarization and depolarization mechanisms discussed above are for the HA compacts which was prepared under the H_2O stream for suppressing OH^- defects. However, in normal air sintering, HA develops defects at OH^- sites on dehydration at elevated temperature.[39,60,61] Various conduction mechanisms such as proton hopping, OH^- as well as O^{2-} diffusion are mediated through OH^- defects.[43,47,56,57,58,62] In addition, the polarization due to the reorientation of the OH^- dipoles has a shorter relaxation time and therefore, unstable at room temperature.[48,49,50] However, HA possesses persistent polarization which influences its interfacial interaction with the biological environment. The development of persistent polarization in defect induced HA has been elucidated with respect to TSDC studies. The obtained TSDC spectra of defect-induced polarized HA, consists of dual peaks.[38] From the TSDC spectra, it can be observed that as polarizing field increases, the peak

intensities of TSDC increase. The lower temperature peak in the TSDC spectra increases linearly with polarizing field according to the eq. (4.9). Therefore, it can be suggested to be associated with the dipolar polarization according to the Langevin-Debye relation.[40] The increase in the peak intensity of the higher peak is exponential with respect to polarizing field and therefore, it can be said to be associated with space charge polarization [eq. 4.10].[41]

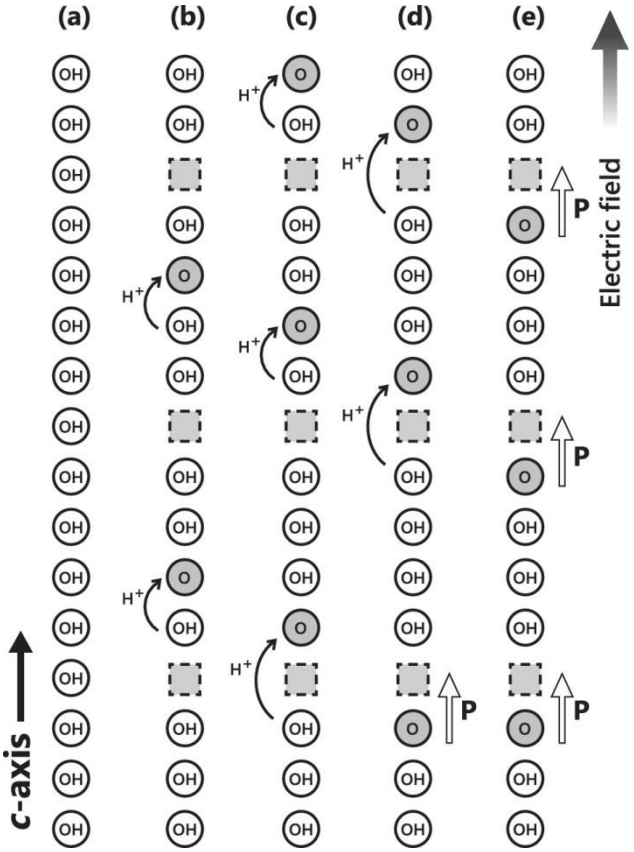

Fig. 4.10: Schematic representation of mechanism of formation of defect pair dipoles: (a) HA crystal having no OH^- defect, (b) creation of OH^- and H^+ defects on dehydroxylation, (c) Subsequent transfer of protons for realignment of defect pair dipoles and (d) aligned defect pair dipoles along the E-field.[38] (Reproduced with permission from AIP publishing)

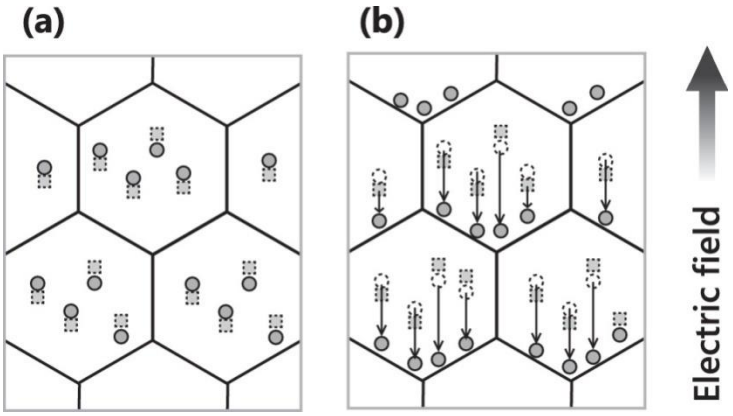

Fig. 4.11: Schematic illustrating the mechanism of space charge formation in HA, (a) proton defects present randomly in the grains, (b) E-field application transfers the protons in the specified direction and accordingly accumulating on the grain boundaries.[38] (Reproduced with permission from AIP publishing)

The dipole polarization model corresponding to the defect concentration is schematically depicted in Fig. 4.10. The OH^- ions are aligned along the c-axis and their orientation can be either up or down with the consideration that HA possesses no OH^- defects [Fig. 4.10(a)]. At elevated temperatures, vacancies of OH^- ions at OH^- site and protons (H^+) on O^{2-} sites are formed in the structure due to the process of dehydroxylation [Fig. 4.10(b)]. The defect at OH^- site renders an effective charge of +1 and the defect at H^+ site renders an effective of charge -1 [Fig. 4.10(b)]. Thereafter, these defect pairs form dipole with random proton transfer. On the application of E-field, the transportation of protons (H^+) in the specified direction takes place, as indicated by solid lines in Fig. 4.10 (c) and (d), thereby, dipoles of defect pairs are consequently aligned along the field direction [Fig. 4.10 (e)]. With the increase of defect concentration, the dipole defect pair increases and henceforth, the dipole polarization also increases. The activation energy of the dipole polarization increases with increased OH^- defects. It is suggested that the formation of defect pair dipole, as illustrated, is the result of proton conduction, as indicated by activation energy value (< 1 eV).[56] The increased activation energy with the increased amount of defect is attributed to the change of

local structure on the introduction of OH^- defects which thereby hinders the mobility of protons.[38]

Fig. 4.11 demonstrates the mechanism of formation of space charge in the crystal structure of HA, after introducing defects. Originally, the defects are produced by the dehydration of the HA structure at elevated temperature.[63] As depicted, the defects are dispersed evenly in the grains [Fig. 4.11(a)]. The applied E-field initiates the movement of the protons in the grains through defects. The doted square box are denoted as proton vacancies and on the application of E-field, these vacancies proceed in the direction, opposite to the applied field. Subsequently, proton transfer takes place in the grains through long distances. Therefore, the protons accumulate near the grain boundaries and this distribution gives rise to space charge polarization [Fig. 4.11(b)]. As defect concentration increases, the density of the mobile protons increases with increase in the number of proton vacancies and as a result, space charge polarization also increases. The activation energy of space charge polarization is independent with respect to the defect concentration.[38] In space charge polarization, activation energy is considered to be the barrier height for trapping and detrapping of charge (H^+), associated with the grain boundaries. The associated activation energy lies in the range of 1.01 - 1.02 eV.[64] It can, therefore, be suggested that persistent polarization in HA comprises of dipolar polarization, associated with the grains and space charge polarization, associated with the grain boundaries.

4.6.3. Dielectric and ac conductivity behaviour of HA

Fig. 4.12(a) represents the variation of dielectric constant and loss with temperature for unpolarized and polarized HA (E_p = 90 kV/cm) at 100 kHz of frequency. The dielectric variation of unpolarized and polarized HA (90 kV/cm) is almost similar (except above 500˚C), indicating that sample chemistry has been preserved even after polarization treatment. The dielectric constant increases with increase in temperature. The significant rise

in the dielectric constant after 100˚C and respective peak in the loss curve for the similar temperature range are associated with the relaxation of space charge and dipolar polarizations for both, the unpolarized and polarized HA.[65,66] The anomalies associated with the dielectric curve in the temperature region of 150 - 250˚C is mainly attributed to the temperature dependent phase transition from monoclinic to hexagonal ($P2_1/b$ to $P6_3/m$) phase.[38,67] In addition, it has been suggested that at the phase transition temperature, the mobility / reorientational motion of OH^- dipoles is abruptly enhanced, however, their adjacent interaction along the column is weak.[68] The increase in the dielectric constant [Fig. 4.12 (a)] after the phase transition temperature represents reorientation of OH^- dipoles along c-axis of the lattice.[66] According to Zakharov et al.[69], above 300˚C, the increase in dielectric constant with temperature is due to the polarization caused by proton (H^+) migration via the formation of thermal defects. It has also been suggested that in the temperature range of 350 - 450˚C, the reorientation of the protons (H^+) of the OH^- ions along c-axis becomes independent of the adjacent OH^- ions in the lattice. This state is dynamically stabilized.[48,49,50] Further, at elevated temperature (> 500˚C), dispersion in the curves of the dielectric constant is observed. Similar dispersion in the loss curve is observed, above 400˚C. It is known that HA depolarizes at the higher temperature (≥ 400˚C), therefore, peak in the loss curve above 500˚C might be associated with the relaxation of space charge in the bulk, trapped under thermal potential barrier as well as of OH^- dipoles. Such response was not observed in the TSDC curve due to its experimental limitations of up to 500˚C. The corresponding downfall in the dielectric curve above 500˚C also represents a similar phenomenon. The significant increase in the dielectric curve above 500˚C and a corresponding decrease in the loss curve for the unpolarized HA can be suggested to be associated with an increase in conduction of protons (H^+) in the bulk.

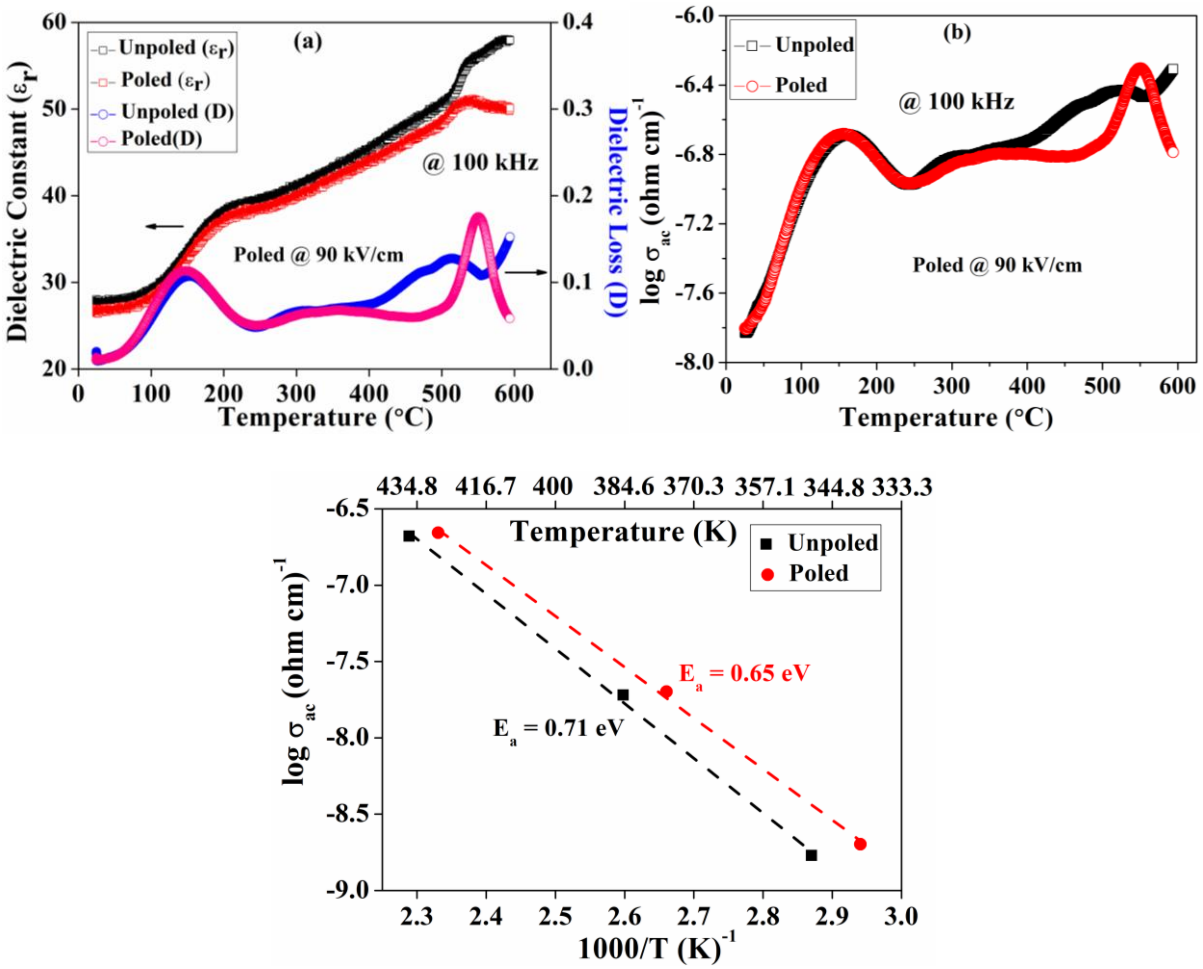

Fig. 4.12: (a) Variation of dielectric constant (ε_r) and loss (D) as well as (b) ac conductivity with temperature at 100 kHz of frequency for the unpolarized and polarized (90 kV/cm) HA. (c) Variation of ac conductivity with inverse of temperature for the unpolarized and polarized HA.

Fig. 4.12 (b) represents the variation of ac conductivity with the temperature at 100 kHz of frequency for unpolarized and polarized HA. For both the samples, the conductivity increases exponentially with temperature up to 150˚C and thereafter, it decreases. After maxima at ~ 150˚C, it shows quasi-linear behaviour for polarized HA up to 500˚C. While, in case of unpolarized counterpart, a slight parabolic behaviour is observed up to 500˚C. The maximum at 150˚C corresponds to the relaxation process which is probably associated with the migration of protons (H^+) in adsorbed water.[66,69] It has been suggested that the hydroxyl

groups, present on the surface of HA attract the water molecules.[70] In addition, the water of hydration forms multiple layers on the HA surface.[71,72] These layers of adsorbed water are gradually dehydrated from the HA surface with temperature (≤ 300˚C) until reaching the dehydroxylation process at the higher temperature (> 500˚C).[73] At low temperature (≤ 200˚C), the adsorbed water facilitates the migration of protons (H^+) through Grotthuss chain reaction in which protons (H^+) conduct through one water molecule to the other on the HA surface.[70] The amount of adsorbed water consequently depends on the surface area. It can, therefore, be suggested that the lower temperature conductivity in HA is due to the proton migration in surface bound water.[57,73] The decrease in conductivity above 150˚C can be attributed to the removal of water of hydration. At higher temperature (> 400˚C), dispersion in both the curves is observed. Similar behaviour is observed in the dielectric (> 500˚C) and loss curve (> 400˚C) [Fig. 4.12(a)]. Fig. 4.12(c) represents the linear variation of conductivity with temperature and appears to follow the Arrehenius relationship [$\sigma = \sigma_o exp(E_a/kT)$], where the parameters, σ_o, E_a, and k is the pre-exponential factor, activation energy and Boltzmann constant, respectively. The activation energy values for the unpolarized and polarized HA are evaluated to be 0.71 eV and 0.65 eV, respectively. The polarization slightly reduced the activation energy values. However, both the values are associated with the proton (H^+) conduction through columnar c-axis in both the samples.[47,74] The dehydroxylation of HA lattice proceeds according to the following reaction,

$$Ca_{10}(PO_4)_6(OH)_2 \rightarrow Ca_{10}(PO_4)_6(OH)_{2-2x}O_x(\square)_x + xH_2O \qquad (4.15)$$

Where, □ indicates vacancies at OH^- sites. The process of dehydroxylation induces hopping of protons (H^+) via $(PO_4)^{3-}$ tetrahedra. This type of conduction is along columnar c-axis. In case of unpolarized HA, as temperature increases, hopping of protons increases via formation of OH^- defects which increases ac conductivity [Fig. 4.12(b)].[47,57,73,75] It has also been suggested that the increased number of vacancies can significantly increase the conductivity

of HA.[23] In case of polarized HA, the maxima above 500˚C corresponds to the relaxation of charges bounded by the thermal potential barrier, while the corresponding decline in the unpolarized counterpart might be associated with the hindrance of the proton (H^+) hopping due to the creation of OH^- ions vacancies.

4.6.4. Influence of polarization on the surface chemistry of HA

Fig. 4.13 represents the X-ray photoelectron spectroscopy (XPS) analyses of unpolarized and polarized (90 kV/cm) HA. The spectra exhibit photoelectron peaks of calcium, oxygen, and phosphorus which are the essential elements, present in HA. The additional photoelectron peaks indicate the presence of adventitious carbon, carbonate and nitrogen on the surface of both, the unpolarized and polarized HA. The carbonate impurity in the XPS spectrum is due to the presence of CO_2 in the air which generally gets absorbed in calcium phosphates in form of carbonate (O-C=O), during their synthesis. In XPS spectra, the binding energy peak, corresponding to carbonate carbon, appears at approximately 287 eV while that of C1s (C-C) is observed at approximately 284 eV for both, the unpolarized and polarized samples. The spectrum of oxygen O1s has been deconvoluted into two additional peaks, representing the contribution from O^{2-} (PO_4^{3-}) and OH^- ions, respectively. However, the peak associated with O1s in the form of O^{2-}(~ 531.2 eV) and OH^- (~ 530.2 eV) ions for unpolarized HA is slightly different from O^{2-} (~ 530.2 eV) and OH^- (~ 531.3 eV) for the polarized counterpart. The atomic percent, evaluated from the peak areas, after smoothening of the plots, are represented in table 4.2. From the atomic percentage for each element present in HA, the Ca/P ratio for unpolarized HA is evaluated to be ~1.42 and that of polarized HA, it is ~1.47. This ratio indicates the presence of pure HA phase on the surface of both, polarized and unpolarized HA i.e., the surface chemistry of HA has not been altered with the exposure of such a high field (90 kV/cm). The atomic ratio of Ca/P, evaluated from the XPS spectra is, however, different from the Ca/P ratio in the pure HA phase (~1.65). This can be due to the presence of

carbonate impurity which readily substitutes the PO_4^{3-} ion and consequently, affects the molar ratio of Ca/P.[76] The Ca/P ratio for HA with carbonate impurity has been reported to be about 1.46.[76] Therefore, the XPS spectra of polarized HA depicts no alteration in its surface chemistry.

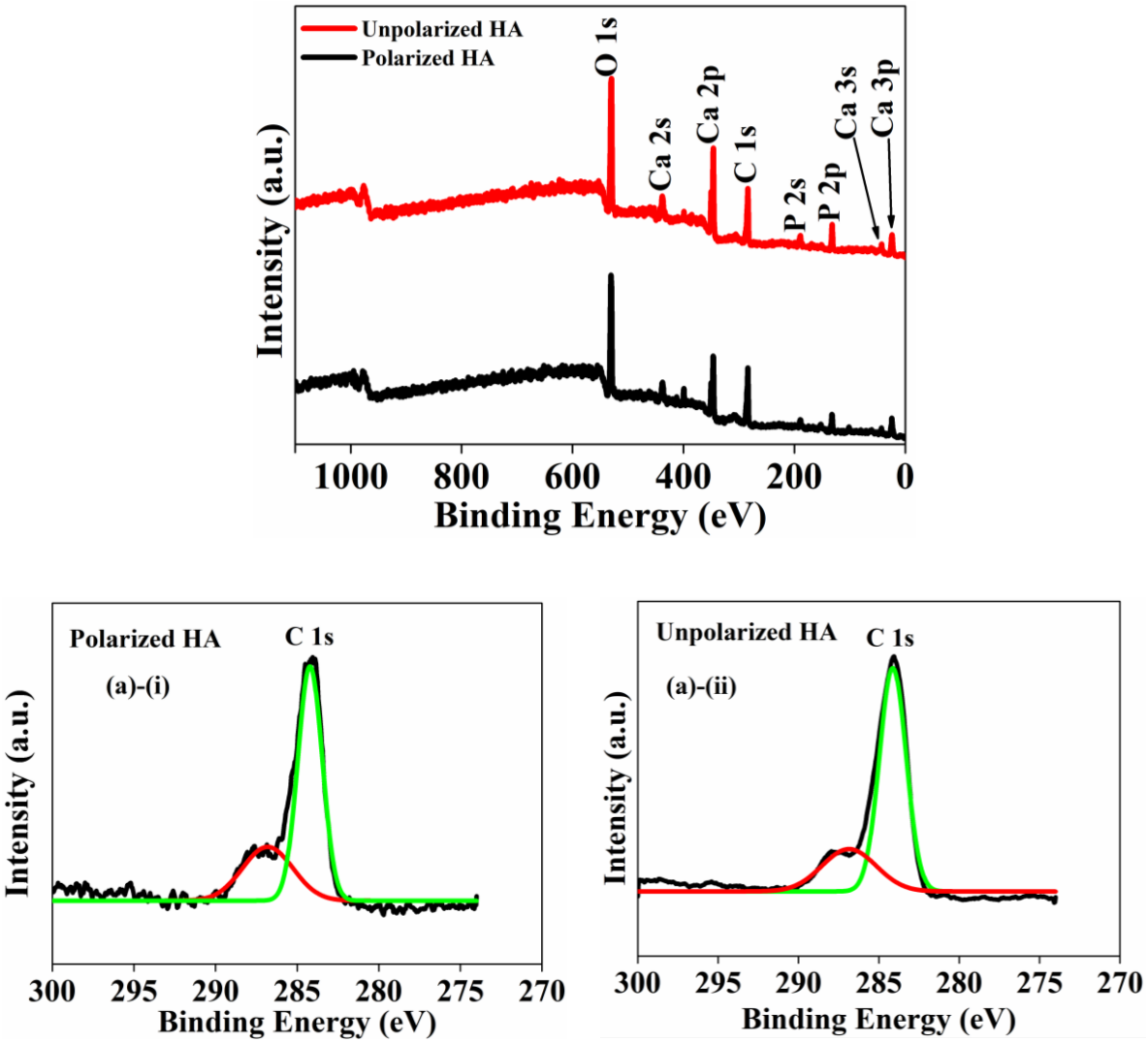

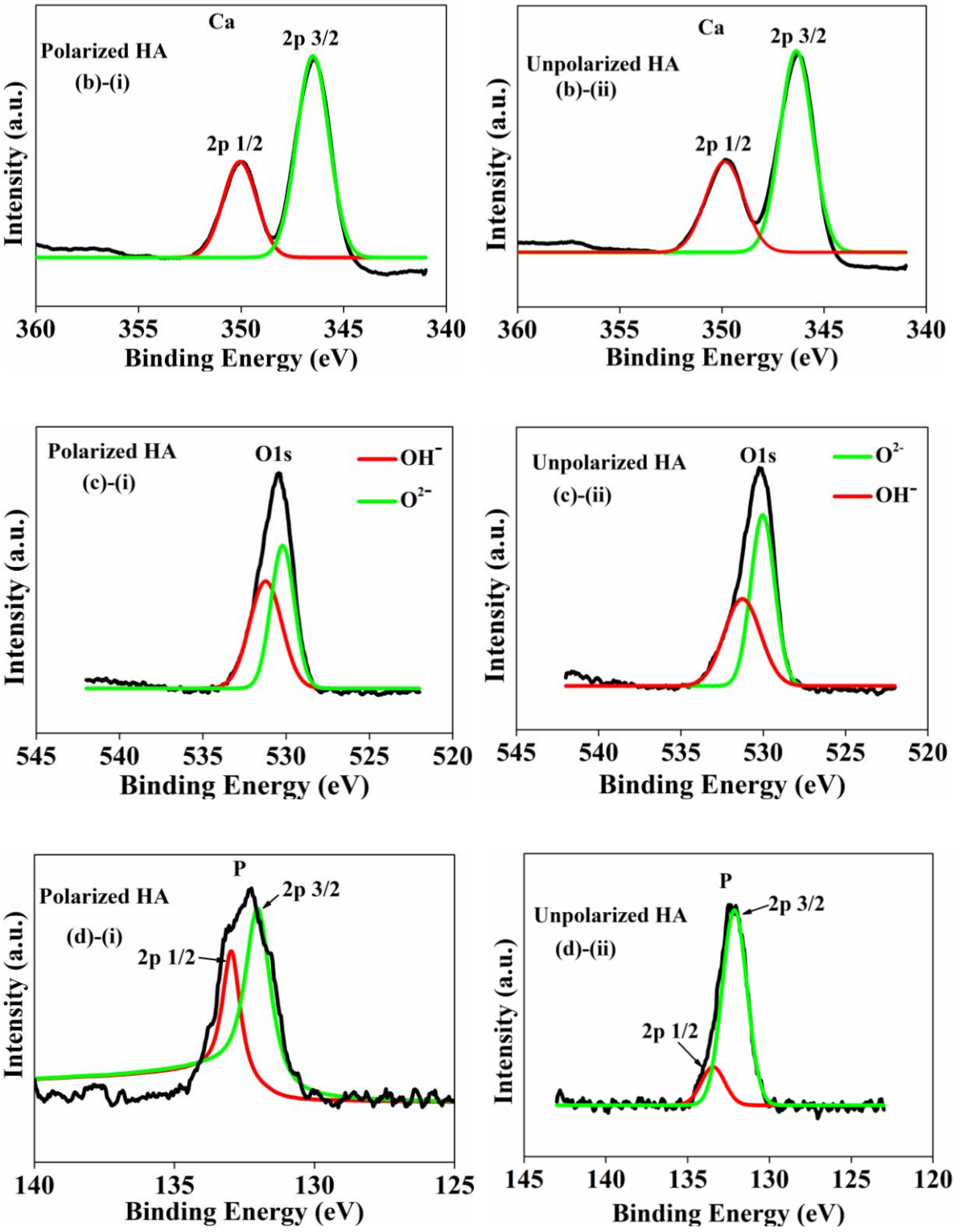

Fig. 4.13: X-ray photoelectron spectroscopy (XPS) spectra of polarized and unpolarized HA. (a)-(i) , (a)-(ii) Adventitious carbon (C-C) along with the presence of O-C=O group is depicted by binding energies of ~ 284 and ~ 287 eV. The presence of (b)-(i), (b)-(ii)

calcium 2p orbital state, (c)-(i),(c)-(ii) Oxygen 1s orbital state and (d)-(i),(d)-(ii) Phosphorus 2p orbital state is depicted in both, the polarized and unpolarized HA.

Table 4.2: Binding energy values for the various elements, present in unpolarized and polarized HA along with their atomic percentage.

Elements		Unpolarized		Polarized	
		B.E. (eV)	Atomic %	B.E. (eV)	Atomic %
C1s	C-C	284.06	25.07	284.1	26.20
	O-C=O	287.1	9.33	287	13.23
Ca2p	$Ca2p_{3/2}$	346.3	12.00	346.5	9.65
	$Ca2p_{1/2}$	349.9	10.80	350	10.67
P2p	$P2p_{3/2}$	132.14	12.67	132.05	10.39
	$P2p_{1/2}$	133.48	3.46	132.9	3.26
O1s	O^{2-}	531.2	26.69	530.2	26.60
	OH^-	530.2		531.3	

4.6.5. TSDC, dielectric and ac conductivity behaviour of NKN

Fig. 4.14 represents the TSDC spectra of polarized NKN. Fig. 4.14 (a) demonstrates the TSDC spectra for the samples, depolarized at a heating rate of 1˚C/min while polarized at 30, 50 and 90 kV/cm, respectively. Fig. 4.14 (b) demonstrates TSDC spectra for the samples, depolarized at heating rates of 1, 5 and 10˚C/min, respectively, while polarized at 90 kV/cm. Both the spectra consist of two sharp peaks. The lower temperature peaks are observed to lie in the temperature range of 200˚C - 300˚C, while higher temperature peaks are observed between 400 - 450˚C [Figs. 4.14 (a) and (b)]. These peaks correspond to the phase transition in the crystal structure of NKN. The lower temperature peak is associated with orthorhombic to tetragonal (T_{O-T}) and high temperature peak is related to tetragonal to cubic (T_C, Curie

point) phase transitions.[77] For NKN samples, polarized at 30 as well as 50 kV/cm and depolarized at a heating rate of 1˚C/min, the orthorhombic to tetragonal phase transition temperature ($T_{O\text{-}T}$) is observed to be at approximately 224˚C [Fig. 4.14 (a)]. However, for the samples, polarized at 90 kV/cm and depolarized at a similar heating rate, $T_{O\text{-}T}$ appears to be shifted to almost 255˚C. In addition, Curie temperature (T_C) for the samples, polarized at 30 and 50 kV/cm is approximately 421˚C, which is lower than that for the samples, polarized at 90 kV/cm (~ 441˚C) [Fig. 4.14 (a)]. However, the samples, polarized at 90 kV/cm and depolarized at the heating rate of 1˚C/min, lower phase transition ($T_{O\text{-}T}$ = 223˚C) and Curie (T_C = 422˚C) temperatures are observed [Figs. 4.14 (b)].

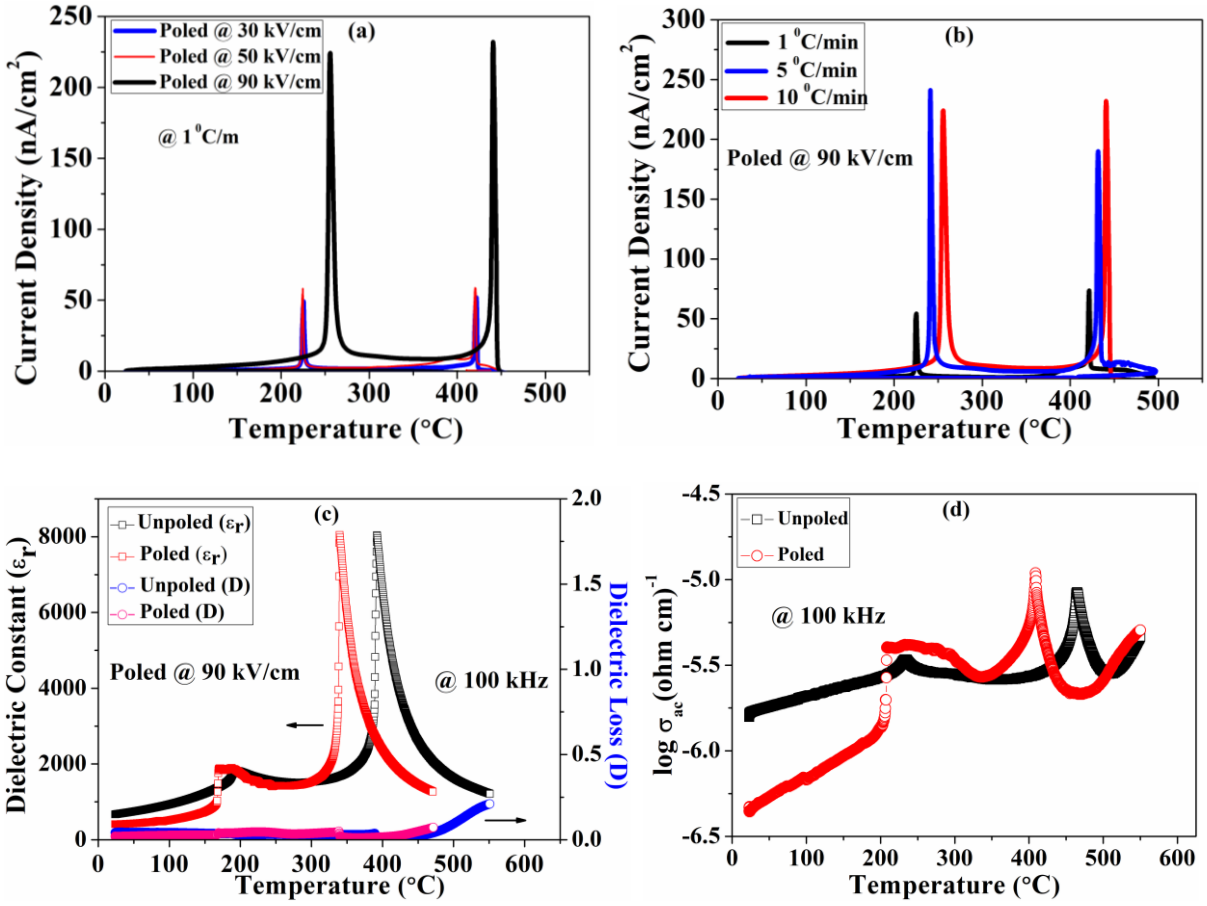

Fig. 4.14: TSDC spectra of $Na_{0.5}K_{0.5}NbO_3$, (a) polarized at 30, 50 and 90 kV/cm, respectively and depolarized at a heating rate of 1˚C/min, (b) polarized at 90 kV/cm and depolarized at heating rates of 1, 5 and 10˚C/min, respectively, (c) variation of dielectric

constant (ε_r) and loss (D) as well as (d) ac conductivity response with temperature at 100 kHz of frequency for unpolarized and polarized $Na_{0.5}K_{0.5}NbO_3$ (90 kV/cm).

The peak current densities (for both phase transition temperatures) for the samples, polarized at 90 kV/cm are much larger than the samples, polarized at 30 as well as 50 kV/cm [Figs. 4.14 (a) and (b)]. Also, for similar TSDC parameters ($E_p \approx 90$ kV/cm and $\beta = 1$˚C/min), the peak current densities (for both transition temperatures) in Fig. 4.14 (a) are significantly larger than those in Fig. 4.14 (b). It is also observed in Fig. 4.14 (b), that the peak current densities during depolarization at heating rates of 5 and 10˚C/min are significantly larger than the peak current densities observed at a heating rate of 1˚C/min. The TSDC spectra of NKN depict sharp current peaks at $T_{O\text{-}T}$ and T_C which is indicative of the pyroelectric currents. Figs. 4.14 (a) and (b) suggest that the pyrocurrent depends on the heating rate (β) as well as the polarizing field (E_p). From the TSDC spectra, it can be concluded that as polarizing field (E_p) is increased from 30 kV/cm to 90 kV/cm, the phase transition temperatures ($T_{O\text{-}T}$, T_C) are shifted towards higher temperature at a similar heating rate (β) during depolarization [Fig. 4.14(a)]. However, for a similar polarizing field, the phase transition temperatures are shifted towards higher temperature with increase in the depolarizing heating rate from 1 to 10˚C/min [Fig. 4.14(b)]. The sintering atmosphere of the NKN ceramics greatly influences their conductive behaviour. This is because alkali metals (Na, K) are highly volatile, and therefore, at elevated temperatures, alkali metal defects are created along with oxygen vacancies through the volatilization process as,[18]

$$2M_M^{\times} + O_O^{\times} \leftrightarrow M_2O\ (gas) + 2V_M' + V_O^{\bullet\bullet} \qquad (4.16)$$

Where, *M* and *V* denote alkali metal and vacancy, respectively. This alkali metal defects along with oxygen vacancy, weakly form defect dipoles ($2V_M^{'}$- $V_O^{\bullet\bullet}$) in air fired NKN

ceramics.[77] After cooling in air atmosphere i.e., superoxidation process, the oxygen vacancies are replaced as,

$$2V_M' + V_O^{\bullet\bullet} + \frac{1}{2}O_2(gas) \leftrightarrow 2V_M' + O_O + 2h^{\bullet} \quad (4.17)$$

Combining eq. (4.16) and (4.17), one can obtain,

$$2M_M + \frac{1}{2}O_2(gas) \leftrightarrow M_2O(gas) + 2V_M' + 2h^{\bullet} \quad (4.18)$$

This process of formation of alkali metal vacancies occurs under the sintering in ambient atmosphere, however, reduced atmosphere sintering i.e., sintering in low pO_2 atmosphere inhibits the formation of alkali metal vacancies. In addition, oxygen vacancies are formed as,

$$O_o \rightarrow \frac{1}{O_2}(gas) + V_o^{\bullet\bullet} + 2e' \quad (4.19)$$

These oxygen vacancies participate in electronic and ionic conduction in the particular perovskite structure of NKN as oxygen ion has activation energy ranging from 0.5 - 2 eV as compared to A-site (4 eV) and B-site (12 eV) ions.[78] Also, the adjacent oxygen ions in the typical perovskite structure are in close proximity (~ 2.8 Å) as compared with that of A-site (~ 4 Å) and B-site (~ 4 Å) ions, which further favours the conduction/migration of oxygen vacancies.[78] Overall, in the typical perovskite structure of NKN, three types of defects can be determined through TSDC i.e., trap charges ($xV_M^{'}$ - $V_o^{\bullet\bullet}$), defect dipole ($2V_M^{'}$- $V_O^{\bullet\bullet}$) and oxygen vacancies ($V_O^{\bullet\bullet}$).[79] Due to the spark plasma sintering route, the formation of alkali metal defects has been suppressed. However, the formation of oxygen vacancies is enhanced in the SPS route. It is also reported that as the partial pressure of oxygen is reduced, energy for the formation of oxygen vacancies is decreased and that of alkali metals is increased.[80,81] Under these conditions, the conduction mechanism in NKN ceramics is of n-type.[18] Also, the formation and migration of oxygen vacancies give rise to space charge conduction.[18] It is

reported that the relaxation or the depolarization current due to space charge in the TSDC spectra can be evaluated from the total developed charge which is further given as,[82]

$$Q_{TSDC} = 2\alpha\upsilon Nqt_p e^{\left(-\frac{H}{kT}\right)} \sinh\left(\frac{q\alpha E_p}{2kT_p}\right) \quad (4.20)$$

$$= Q_o \sinh(q\alpha E_p/2kT_p)$$

Where, q is the ionic charge, N is the charge density, υ is the hopping/migration frequency, H is the potential barrier height, k is the Boltzmann constant, T_p is the polarization temperature and E_p is the polarization field. It is reported that the TSDC spectra of $SrTiO_3$ crystals consist of three consecutive peaks.[83] Each peak is correlated via polarizing temperature (T_p) and peak temperature (T_m). Therefore, in the TSDC spectra of $SrTiO_3$ crystal, increase in T_p with the corresponding decrease in T_m can be suggested to be associated with the relaxation of trap charge. Secondly, an increase in T_p results in the rise of T_m which is correlated with relaxation/migration of oxygen vacancies. Thirdly, when there is no effect of increasing T_p on T_m, the relaxation phenomenon is suggested to be associated with the defect dipoles. In case of polycrystalline $SrTiO_3$, relaxation due to migration oxygen vacancies across grain boundaries also contributes to the TSDC spectra along with the above-mentioned relaxation phenomenon.[82] It is also reported that the NKN defect structures are closely related to $SrTiO_3$ samples.[78] Further, it has been reported that the reduced atmosphere fired NKN with oxygen vacancies have degraded piezoelectricity as well as ferroelectricity because of the accumulation of oxygen vacancies in grain boundaries under the polarizing field.[79,82] However, in the SPSed sample, oxygen vacancies are closely related to the post-annealing temperature and time.[84]

Fig. 4.14 (c) represents the temperature dependent dielectric behaviour of the unpolarized and polarized NKN ceramics at a frequency of 100 kHz. It can be observed that there are two anomalies in the dielectric behaviour of both the samples.[85,86] The first anomaly is related to

the ferroelectric orthorhombic to ferroelectric tetragonal phase transition at the temperature of 195˚C (T_{O-T}) for the unpolarized NKN in contrast to the temperature of 171˚C for the polarized counterpart. The second anomaly is analogous to ferroelectric tetragonal to paraelectric cubic phase transition (T_C) at a temperature of 393˚C for the unpolarized NKN in contrast to that of 338˚C for its polarized counterpart.[87] Both, the transition temperatures shifted to lower temperature region for the polarized NKN as compared with that of the unpolarized NKN. However, the dielectric behaviour of both the samples is almost similar. This indicates that under such a high polarizing E-field (~ 90 kV/cm), the sample chemistry, as well as bulk properties of the NKN, have been preserved. The low values of the dielectric losses are associated with the reasonably good sintering and dense microstructure of the SPSed samples.[88]

Fig. 4.14 (d) represents the temperature dependent ac conductivity behaviour of unpolarized and polarized NKN ceramics at a frequency of 100 kHz. The ac conductivity plot exhibits two anomalies (T_{O-T} and T_C) similar to the dielectric and TSDC characteristics. The first anomaly at ~ 233˚C for the unpolarized and at ~ 209˚C for the polarized NKN represents the ferroelectric orthorhombic to ferroelectric tetragonal phase transition (T_{O-T}).[89] The higher temperature anomaly at ~ 468˚C for the unpolarized and ~ 409˚C for the polarized NKN represents the ferroelectric tetragonal to paraelectric cubic phase transition (T_C).[90] It is observed that the conductivity of the polarized NKN is lower than the unpolarized counterpart (before T_{O-T}). Thereafter, the conductivity of the unpolarized and polarized NKN sample shows similar behaviour before their respective T_C values. SPSed samples possess dense microstructure as alkali metal defects have been suppressed. However, oxygen vacancies are formed which gives rise to n-type conduction in the samples.[18,77,89,90] Also, above T_C, a sudden rise in the conductivity curve for both, unpolarized and polarized NKN is observed. This is because of the enhanced conduction of mobile ions (oxygen vacancies and

n-type charge carriers) which have gained sufficient energy.[91] This behaviour is suggestive of the negative temperature coefficient of resistance (NTCR) like that of semiconductors.[91] In addition, it is observed that the T_{O-T} and T_C of the polarized NKN are shifted to lower temperature as compared to its unpolarized counterpart, as mentioned earlier.

4.6.6. TSDC, dielectric and ac conductivity behaviour of HA-25 vol % NKN composite

Fig. 4.15 (a) represents the TSDC spectra of polarized (90 kV/cm) HA-25 vol % NKN composite, depolarized at various heating rates of 1, 5 and 10 °C/min. In the TSDC spectra, multiple peaks can be observed for depolarization at heating rates of 1 and 10 °C/min. For depolarization at 5 °C/min, negative current density peak is observed at ~ 370 °C. In addition, the other relaxation peak is observed above 400 °C. The negative current density peak can be described from the context of simultaneous presence of hetero and homocharges in the TSDC experiment.[37] Heterocharges are due to the internal polarization of the sample while homocharges are of extrinsic origin which occurs due to the excessive high polarization field (E_p).[37] Generally, the relaxation of these charges occur simultaneously resulting in unidirectional flow of current, however, if the relaxation of these charges differ, current can flow in the opposite direction which can be observed in the TSDC spectra [Fig. 4.15(a)].[37] As the amount of reinforcement phase i.e., NKN is comparatively low, therefore, the polarization of HA-25 NKN composite is dominantly due to HA phase. This is due to the broad curves in the TSDC spectra depicting a thermoelectret nature of the sample as compared with that of sharp peaks suggested being of ferroelectric material.[43,92,93,94,95] Table 4.3, depicts the charge density stored in the HA-25 NKN which are significantly larger than the charge density of monolithic HA. For depolarization at 10 °C/min, peak at ~ 500°C is due to the heating of the sample while peak at ~ 416°C is appearing in the cooling phase. Therefore, table 4.3 depicts the total charge density during depolarization at 10° C/min. The presence of reinforcement phase in the matrix (HA) can be recognized in the TSDC spectra as relatively small peaks are

observed near the phase transition temperatures (T_{O-T}, T_C) of NKN. As mentioned above, due to the temperature limitation of the TSDC set up, there is an incomplete depolarization of HA-25 NKN composite. It is known that NKN exhibits spontaneous polarization due to its ferroelectric nature which imparts piezoelectric nature to the HA-25 NKN composite. In addition, HA is brittle in nature and its fracture toughness is comparatively low with that of a bone tissue. The addition of NKN as a piezoelectric secondary phase can significantly increase the fracture toughness of the composite.[96,97] It has been reported that the HA along with the piezoelectric secondary phase possesses enhanced electromechanical characteristics.[22]

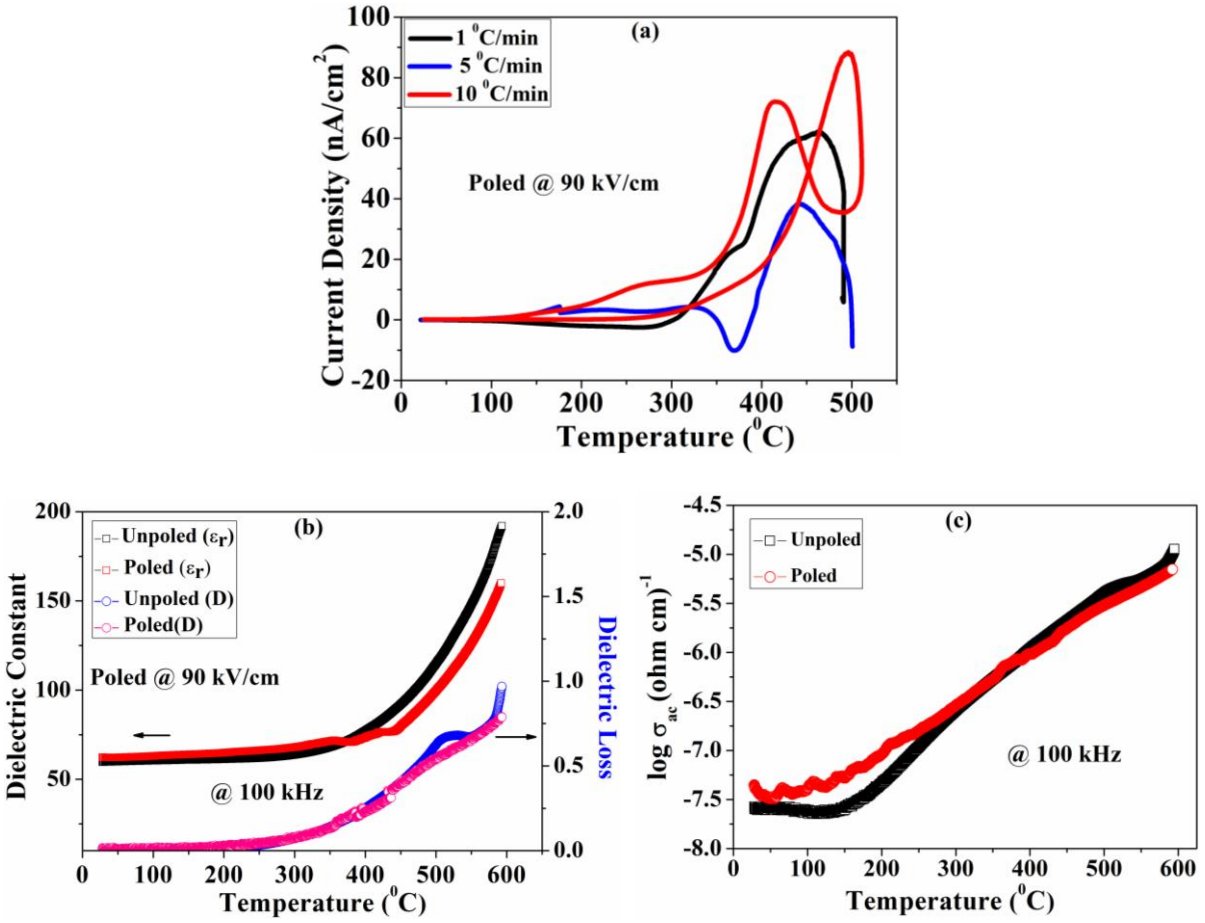

Fig. 4.15: (a) TSDC spectra of HA-25 vol % NKN composite, polarized at 90 kV/cm, (b) dielectric constant (ε_r) and loss (D) as well as (c) ac conductivity behaviour with

temperature at 100 kHz of frequency for unpolarized and polarized HA-25 vol% NKN composite.

Table 4.3: Depolarization response of HA-25 NKN composite as a function of heating rate.

Polarizing E-field (E_p) (90 kV/cm)	Charge Density (Q_p)	Peak Temperature (T_{max})	Peak Current density (J_{max})	Heating Rate (β)
	6.4 μC/cm^2	464.62 °C	61.5 nA/cm^2	1 °C/min
	0.67 μC/cm^2	443.6 °C	38.2 nA/cm^2	5 °C/min
	1.6 μC/cm^2	418.28 °C	71.9 nA/cm^2	10 °C/min

Fig. 4.15 (b) represents the dielectric and loss characteristics of unpolarized and polarized (90 kV/cm) HA-25 vol % NKN composite with temperature at 100 kHz. The dielectric constant and loss behaviour is almost independent with temperature upto 300 °C. Thereafter, there is an increase in dielectric response for unpolarized as well as polarized (90 kV/cm) HA-25 vol % NKN composite. For both the samples, the characteristics are almost similar indicating that there is no alteration in the sample chemistry under such a high polarizing field (90 kV/cm). The room temperature dielectric constant values for unpolarized and polarized HA-25 NKN composites are ~ 60 and ~ 62 which are significantly higher as compared to the room temperature value of dielectric constant for the monolithic HA (~ 25). Therefore, the addition of NKN in the HA matrix has increased the polarizability of the composite. The room temperature loss values are quite low (~ 0.008) indicating that the NKN phase has been well processed with HA phase. In addition, after SPS, the density of the compacts was almost 99%. The monotonous increase in the dielectric and loss characteristics of unpolarized sample depicts the reorientation of OH^- dipoles in the HA phase. It needs to be mentioned that although the polarizability has been increased with the addition of the piezoelectric phase

with the HA, but the excellent biocompatibility of HA with the bone tissue might be influenced.

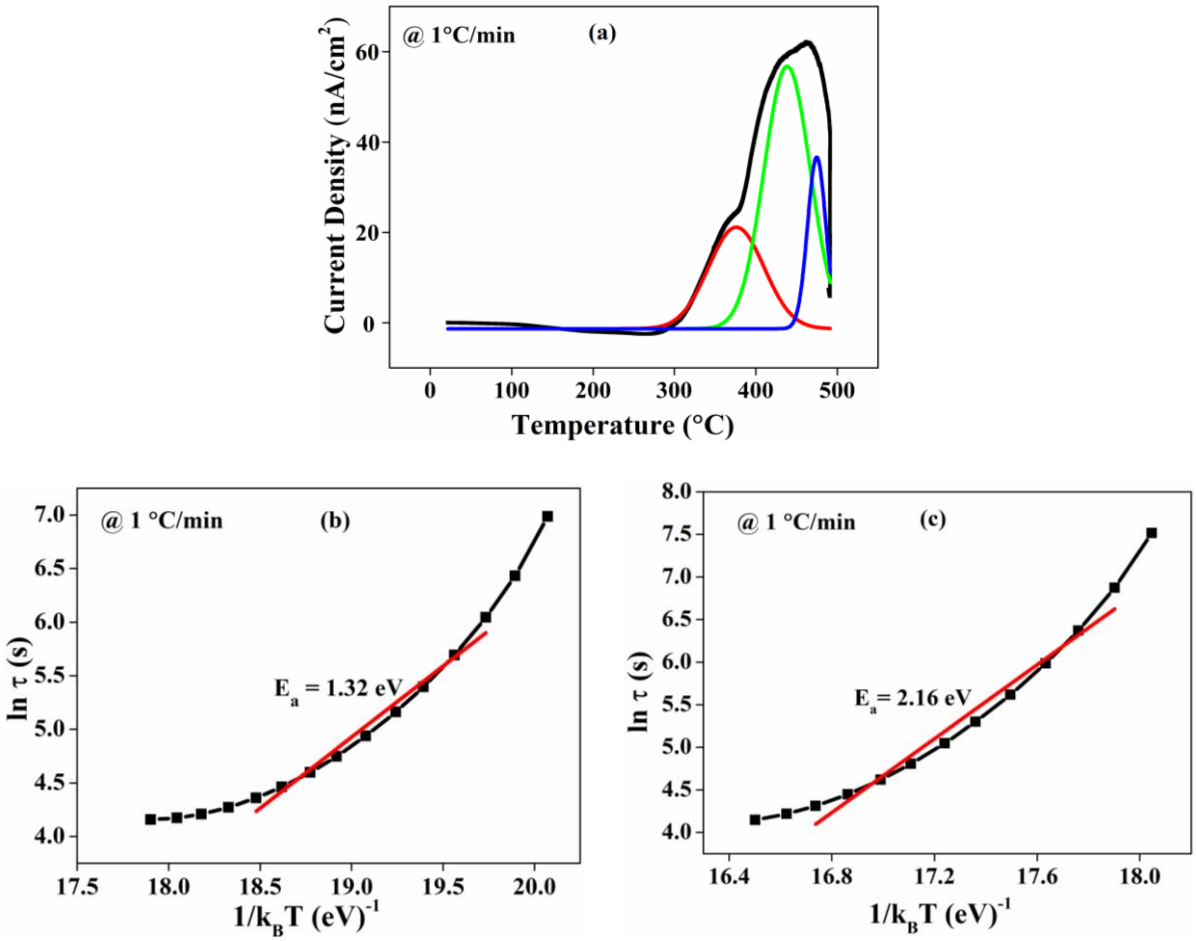

Fig. 4.16: Deconvoluted TSDC spectra of HA-25 vol % NKN composite, depolarized at the heating rate of 1°C/min. The respective Arrhenius plots (b) and (c) depicting activation energies of deconvoluted spectra.

Fig. 4.15 (c) represents the ac conductivity behaviour of unpolarized and polarized (90 kV/cm) HA-25 vol % NKN composite with temperature at 100 kHz of frequency. The ac conductivity behaviour for both the samples is almost similar above 250˚C. A slight difference in the ac conductivity behaviour is observed between both samples upto 250 °C. It can be associated with the enhanced electroactive nature of polarized HA-25 NKN composite. The conductivity of the composite at room temperature is obtained to be about ~

10^{-7} (ohm cm)$^{-1}$ in contrast to that of ~ 10^{-8} (ohm cm)$^{-1}$ for pure HA. This suggests that with the addition of NKN in HA, there is no significant rise in the conductivity of HA-25 NKN composite.

It can be observed in Fig. 4.16 (a) that the TSDC spectra, for depolarization at 1°C/min, represent peaks depicting multiple relaxation mechanisms. Consequently, in Fig. 4.16(a), three deconvoluted peaks for depolarization at 1°C/min are observed. The associated activation energies for the first two peaks are 1.32 eV and 2.16 eV, respectively. The activation energy associated with the third deconvoluted peak cannot be determined due to the incomplete depolarization.

4.7. Summary

High polarizing field (~ 90 kV/cm) have a vital impact over the electrical behaviour of SPSed HA and ferroelectric NKN. The TSDC results suggest that the amount of charge stored in HA increases with increase in polarizing field upto 90 kV/cm. The dielectric behaviour of HA, polarized at 90 kV/cm is almost similar to that of unpolarized counterpart, upto 500˚C. The activation energy values suggest that the proton conduction/migration in unpolarized as well as polarized HA is the primary reason for conduction. For ferroelectric NKN, high polarizing field (~ 90 kV/cm) have shifted their phase transition temperatures towards the higher temperature region. The prominent conduction in both, the unpolarized and polarized NKN is due to the migration of oxygen vacancies as well as n-type charge carriers. The surface characteristics, studied through XPS for unpolarized and polarized HA (~ 90 kV/cm), revealed no alteration in the surface chemistry after polarization treatment with such a high field intensity.

References

[1] C. J. Dreyer, "Properties of Stressed Bone", *Nature*, 190: (1961), 1217.

[2] F. R. Baxter, C. R. Bowen, I. G. Turner, and A.C.E. Dent., "Electrically active bioceramics: a review of interfacial responses", *Annals of Biomedical Engineering*, 38(6), (2010), 2079 - 2092.

[3] G.W. Hastings and F.A. Mahmud, "Electrical effects in bone", *Journal of Biomedical Engineering*, 10, (1988), 515-521.

[4] J. Jacob, N. More, K. Kalia, and G. Kapusetti, *"*Piezoelectric smart biomaterials for bone and cartilage tissue engineering", *Inflammation and Regeneration*, 38:2, (2018).

[5] TL Arinzeh, N. Weber and M. Jaffe, "Electrospun electroactive polymers for regenerative medicine applications. In: Google Patents; 2016.

[6] B. Miara, E. Rohan, M. Zidi and B. Labat, "Piezomaterials for bone regeneration design—homogenization approach", *Journal of the Mechanics and Physics of Solids*, 53(11): (2005), 2529-56.

[7] D. Kumar, J. P. Gittings, I. G. Turner, C.R. Bowen, L.A. Hidalgo-Bastida and S.H Cartmell, "Polarization of hydroxyapatite: Influence on osteoblast cell proliferation", *Acta Biomaterialia*, 6, (2010), 1549-1554.

[8] S. Bodhak, S. Bose, and A. Bandyopadhyay, "Role of surface charge and wettability on early stage mineralization and bone cell–materials interactions of polarized hydroxyapatite", *Acta Biomaterialia*, 5, (2009), 2178–2188.

[9] J. B. Park, B. J. Kelly, G. H. Kenner, A. F. von Recum, M. F. Grether, and W. W. Coffeen, "Piezoelectric ceramic implants: *in vivo* results", *Journal of Biomedical Materials Research*, 15, (1981), 103-110.

[10] J. B. Park, A. F. von Recum, G. H. Kenner, B. J. Kelly, W. W. Coffeen, and M. F. Grether, "Piezoelectric ceramic implants: A feasibility study", *Journal of Biomedical Materials Research*, 14, (1980), 269-277.

[11] N. More and G. Kapusetti, "Piezoelectric material - A promising approach for bone and cartilage regeneration", *Medical Hypotheses*, 108, (2017), 10-16.

[12] C. Ribeiro, D. M. Correia, I. Rodrigues, L. Guardão, S. Guimarães, R. Soares and S. Lanceros-Méndez, "In-vivo demonstration of the suitability of piezoelectric stimuli for bone reparation", *Materials Letters*, 209, (2017), 118-121.

[13] D. Khare, B. Basu and A. K. Dubey, "Electrical stimulation and piezoelectric biomaterials for bone tissue engineering applications", *Biomaterials*, 258, (2020), 120280.

[14] K. Kapat, Q. T. H. Shubhra, M. Zhou and S. Leeuwenburgh, "Piezoelectric Nano-Biomaterials for Biomedicine and Tissue Regeneration", *Advanced Functional Materials*, (2020), 1909045.

[15] G. Murillo, A. Blanquer, C. Vargas-Estevez, L. Barrios, E. Ibáñez, C. Nogues, J. Esteve, "Electromechanical Nanogenerator-Cell Interaction Modulates Cell Activity", *Advanced Materials*, 29, (2017), 1605048.

[16] K. Nilsson, J. Lidman, K. Ljungstrom, and C. Kjellman, "Biocompatible material for implants", *U.S. patent 6*, 526, 984 B1, (2003).

[17] K. Kakimoto, Y. Hayakawa, and I. Kagomiya, "Low-temperature sintering of dense (Na,K)NbO_3 piezoelectric ceramics using the citrate precursor technique", *Journal of the American Ceramic Society*, 93, (2010), 2423-2426.

[18] K. Kobayashi, Y. Doshida, Y. Mizuno, and C. A. Randall, "A Route Forwards to Narrow the Performance Gap between PZT and Lead-Free Piezoelectric Ceramic with Low Oxygen Partial Pressure Processed $(Na_{0.5}K_{0.5})NbO_3$", *Journal of the American Ceramic Society*, 95, (2012), 2928-2933.

[19] J. Abe, M. Kobune, K. Kazuya, Y. Tetsuo, H. Masumoto and T. Goto, "Effects of spark-plasma sintering on the piezoelectric properties of high-density (1-x)($Na_{0.5}K_{0.5}$)NbO_3-x$LiTaO_3$ ceramics", *Journal of the Korean Physical Society,* 51(2), (2007), 810-814.

[20] Y. W. Gu, N. H. Loh, K. A. Khor, S. B. Tor and P. Cheang, "Spark plasma sintering of hydroxyapatite powders", *Biomaterials*, 23(1), (2002), 37-43.

[21] A. K. Dubey, P. K. Mallik, S. Kundu and B. Basu, "Dielectric and electrical conductivity properties of multi-stage spark plasma sintered HA-$CaTiO_3$ composites and comparison with conventionally sintered materials", *Journal of the European Ceramic Society*, 33 (15-16), (2013), 3445-3453.

[22] A .K. Dubey, K. Balani and B. Basu, "Multifunctional Properties of Multistage Spark Plasma Sintered HA–$BaTiO_3$-Based Piezobiocomposites for Bone Replacement Applications.", *Journal of the American Ceramic Society*, 96: (2013), 3753-3759.

[23] J. Sans, J. Liora, V. Sanz, J. Puiggali, P. Turon and C. Aleman, "Electrically Polarized Hydroxyapatite: Influence of the Polarization Process on the microstructure and properties", *Langmuir* 35 (46), (2019), 14782-14790.

[24] M. Rivas, L. J. Del Valle, E. Armelin, O. Bertran, P. Turon, J. Puiggali and C. Aleman, "Hydroxyapatite with permanent electrical polarization: Preparation, Characterization and Response Against Inorganic Absorbates", *ChemPhysChem*, 19, (2018), 1746.

[25] S. Li, H. Izui, and M. Okano, "Densification, Microstructure, and Behavior of Hydroxyapatite Ceramics Sintered by Using Spark Plasma Sintering", ASME. *Journal of Engineerng Materials and Technol*ogy, 130(3): (2008), 031012.

[26] C. Bucci, R. Fieschiand and G. Guidi, "Ionic Thermocurrents in Dielectrics", *Physical Review Letters*, 148, (1966), 816.

[27] M. Davies, P. J. Hains, and G. Williams, "Molecular motion in the supercooled liquid state: ion pairs in slow motion", *Journal of the Chemical Society, Faraday Transactions 2: Molecular and Chemical Physics*, 69, (1973), 1785-1792.

[28] T. Hino, "Measurement of dipolar relaxation times and dielectric constants using thermally stimulated current", *Journal of Applied Physics*, 46, (5), (1975), 1956-1960.

[29] M. Zielińskiand and M. Kryszewski, "Thermal sampling technique for the thermally stimulated discharge in polymers model calculations", *physica status solidi (a)*, 42, (1977), 305-314.

[30] I. Diaconu and Sv. Dumitrescu, "Investigations on electric properties of polymers—II. Dielectric relaxation in atactic polystyrene determined by thermally stimulated depolarization currents", *European Polymer Journal*, 14(11), (1978), 971-975.

[31] C. Lacabanne, P. Goyaud and R. F. Boyer, "Thermally stimulated current (TSC) study of the T_g and T_{ll} transitions in anionic polystyrenes", *Journal of Polymer Science: Polymer Physics Edition*, 18, (1980), 277-284.

[32] S.K. Shrivastava, J.D. Ranade, A.P. Srivastava, "Thermally stimulated discharge currents in polystyrene films", *Thin Solid Films*, 67 (2), (1980), 201-206.

[33] A. Gourari, M. Bendaoud, C. Lacabanne and R. F. Boyer, "Influence of tacticity on T_β, T_g, and T_{LL} in poly(methyl methacrylate)s by the method of thermally stimulated current (TSC)", *Journal of Polymer Science: Polymer Physics Edition*, 23, (1985), 889-916.

[34] F. H. Abd El-Kader , A. M. Shehap , M. S. Abo-Ellil and K. H. Mahmoud, "Relaxation phenomenon of poly(vinyl alcohol)/sodium carboxy methyl cellulose blend by thermally stimulated depolarization currents and thermal sample technique", *Journal of Applied Polymer Science*, 95, (2005), 1342-1353.

[35] K. Sato, T. Koizumi and K. Okajima, "Analysis of Ice Water by the Thermally Stimulated Depolarized Current (TSDC) Method", *Analytical Sciences*, 21, (2005), 331-335.

[36] A. K. Dubey, H. Yamada and K. Kakimoto, "Space charge polarization induced augmented in vitro bioactivity of piezoelectric (Na, K) NbO_3", *Journal of Applied Physics*, 114, (2013), 124701.

[37] J. Vanderschueren and J. Gasiot, "Field-induced thermally stimulated currents". In: Bräunlich P. (eds) Thermally Stimulated Relaxation in Solids. Topics in Applied Physics, vol 37. Springer, Berlin, Heidelberg, 1979.

[38] N. Horiuchi, M. Nakamura, A. Nagai, K. Katayama and K. Yamashita, "Proton conduction related electrical dipole and space charge polarization in hydroxyapatite", *Journal of Applied Physics*, 112, (2012), 074901.

[39] C. J. Liao, F. H. Lin, K. S. Chen and J. S. Sun, "Thermal decomposition and reconstitution of hydroxyapatite in air atmosphere", *Biomaterials*, 20 (19), (1999), 1807-1813.

[40] W.T. Coffey, "On the Derivation of Debye Theory of dielectric relaxation from the Langevin equation in the presence of the driving field", *The journal of Chemical Physics*, 93, (1), (1990), 724-729.

[41] J. C. Elliott, "Structure and Chemistry of the Apatites and Other Calcium Orthophosphates", Elsevier, Amsterdam, 1994.

[42] Y. González-Abreu, A. Peláiz-Barranco, A. C. Garcia-Wong, and J. D. S. Guerra, "The pyroelectric behavior of lead free ferroelectric ceramics in thermally stimulated depolarization current measurements", *Journal of Applied Physics*,111, (2012), 124102.

[43] S. Nakamura, H. Takeda and K. Yamashita, "Proton transport polarization and depolarization of Hydroxyapatite ceramics", *Journal of Applied Physics*, 89, (2001), 5386-5392.

[44] J. Acker, H. Kungl, R. Schierholz, S. Wagner, R.-A. Eichel and M. J. Hoffmann, "Microstructure of sodium-potassium niobate ceramics sintered under high alkaline vapor pressure atmosphere", *Journal of the European Ceramic Society*, 34, (2014), 4213-4221.

[45] Y. Tanaka, T. Iwasaki, M. Nakamura, A. Nagai, K. Katayama and K. Yamashita, "Polarization and microstructural effects of ceramic hydroxyapatite electrets", *Journal of Applied Physics*, 107, (2010), 014107.

[46] S. Kasamatsu and O. Sugino, "First-principles investigation of polarization and ion conduction mechanisms in Hydroxyapatite", *Physical Chemistry Chemical Physics*, 20, (2018), 8744 -8752.

[47] K. Yamashita, K. Kitagaki, and T. Umegaki, "Thermal Instability and Proton Conductivity of Ceramic Hydroxyapatite at High Temperatures", *Journal of the American Ceramic Society*, 78, (1995), 1191-1197.

[48] N. Hitmi, D. Chatain, C. Lacabanne, J. Dugas, J.C. Trombe, C. Rey and G. Montel, "TSC study of dipolar reorientations in hydroxyapatites", *Solid State Communications*, 33 (9), (1980), 1003-1004.

[49] N. Hitmi, E. L. Plaino, A. Lamure, C. LaCabanne, and R.A. Young, "Reorientable electric dipoles and cooperative phenomena in human tooth enamel", *Calcified Tissue International*, 38 (5), (1986), 252-261.

[50] N. Hitmi, C. LaCabanne and R.A. Young, "OH^- dipole reorientability in hydroxyapatites: Effect of tunnel size", *Journal of Physics and Chemistry of Solids*, 47 (6), (1986), 533-546.

[51] H. B. V. Rees, M. Mengeot and E. Kostiner, "Monoclinic-hexagonal transition in hydroxyapatite and deuterohydroxyapatite single crystals", *Materials Research Bulletin*, 8 (11), (1973), 1307-1309.

[52] T. Ikoma, A. Yamazaki, S. Nakamura and M.Akao, "Phase Transition of Monoclinic Hydroxyapatite", *Netsu Sokutei*, 25(5), (1998), 141-149.

[53] H. Suda, M. Yashima, M. Kakihana and M. Yoshimura, "Monoclinic .tautm. Hexagonal Phase Transition in Hydroxyapatite studied by X-ray Powder Diffraction and Differential

Scanning Calorimeter Techniques", *Journal of Physical Chemistry*, 99, 17, (1995), 6752-6754.

[54] K. Yamashita, H. Owada, H. Nakagawa, T. Umegakiand T. Kanazawa, "Trivalent Cation Substituted Calcium Oxyhydroxyapatite", *Journal of the American Ceramic Society*, 69, (1986), 590-594.

[55] B. S. Royce, "Field Induced Transport Mechanisms in Hydroxyapatite", *Annals of the New York Academy of Sciences*, 238, (1974), 131-138.

[56] G. C. Maiti and F. Friedemann, "Influence of fluorine substitution on the proton conductivity of hydroxyapatite", *Journal of Chemical Society, Dalton Transactions*, 0, (1981), 949-955.

[57] J.P. Gittings, C.R. Bowen, A.C.E. Dent, I.G. Turner, F.R. Baxter and J.B. Chaudhuri, "Electrical characterization of hydroxyapatite-based bioceramics", *Acta Biomaterialia*, 5 (2), (2009), 743-754.

[58] M. Ueshima, S. Nakamura and K. Yamashita, Huge, "Millicoulomb Charge Storage in Ceramic Hydroxyapatite by Bimodal Electric Polarization", *Advanced Materials*, 14, (2002), 591-595.

[59] K. Yamashita, H. Owada, T. Umegaki, T. Kanazawa and T. Futagami, "Ionic conduction in apatite solid solutions", *Solid State Ionics*, 28–30, (1), (1988), 660-663.

[60] H. Fujimori, H. Toya, K. Ioku, S. Goto and M. Yoshimura, "In situ observation of defects in hydroxyapatite up to 1200°C by ultraviolet Raman spectroscopy", *Chemical Physics Letters*, 325 (4), (200), 383-388.

[61] K. Yamashita, K. Kitagaki, T. Umegaki and T. Kanazawa, "Effects of Sintering ambient H_2O vapour on the protonic conduction properties of ceramic hydroxyapatite", *Journal of Materials Science Letters* 10, (1991), 4-6.

[62] K. Yamashita, N. Oikawa and T. Umegaki, "Acceleration and Deceleration of Bone-Like Crystal Growth on Ceramic Hydroxyapatite by Electric Poling", *Chemistry of Materials* 8 (12), (1996), 2697-2700.

[63] H. Fujimori, H. Toya, K. Ioku, S. Goto and M. Yoshimura, "In situ observation of defects in hydroxyapatite up to 1200°C by ultraviolet Raman spectroscopy", *Chemical Physics Letters*, 325 (4), (2000), 383-388.

[64] M. Nakamura, A. Nagai, Y. Tanaka, Y. Sekijima and K. Yamashita, "Polarized hydroxyapatite promotes spread and motility of osteoblastic cells", *Journal of Biomedical and Materials Research*, 92 A, (2010), 783-790.

[65] V. P. Orlovskii, N. A. Zakharov and A. A. Ivanov, "Structural transition and dielectric characteristics of high-purity hydroxyapatite", *Inorganic Materials* 32(6), (1996), 654-656.

[66] A. K. Dubey, K. Kakimoto, A. Obata and T. Kasuga, "Enhanced polarization of hydroxyapatite using the design concept of functionally graded materials with sodium potassium niobate", *RSC Advances,* 4, (2014), 24601-24611.

[67] N.A. Zakharov, "An analysis of the phase transitions in biocompatible $Ca_{10}(PO_4)_6(OH)_2$", *Technical Physics Letters* 27, (2001), 1035.

[68] N. Horiuchi, N. Wada, K. Nozaki, M. Nakamura, A. Nagai and K. Yamashita, "Dielectric relaxation in monoclinic hydroxyapatite: Observation of hydroxide ion dipoles", *Journal of Applied Physics* 119, (2016), 084903.

[69] N. A. Zakharov and V.P. Orlovskii, "Dielectric characteristics of biocompatible $Ca_{10}(PO_4)_6(OH)_2$ ceramics", *Technical Physics Letters* 27(8), (2001), 629-631.

[70] R. E. Newnham, "Electroceramics", *Reports on Progress in Physics* 52, (1989), 123-156.

[71] H. M Rootare and R. G. Craig, "Vapor phase adsorption of water on hydroxyapatite", *Journal of Dental Research* 56: (1977), 1437-1488.

[72] M. Markovic, B. O. Fowler and M. S. Tung, "Preparation and comprehensive characterisation of a calcium hydroxyapatite reference material", *Journal of Research of the National Institute of Standards and Technology* 109: (2004), 553-568.

[73] M. Nagai and T. Nishino, "Surface conduction of porous hydroxyapatite ceramics at elevated-temperatures", *Solid State Ionics* 28– 30, (1988), 1456-1461.

[74] N. Horiuchi, J. Endo, N. Wada, K. Nozaki, M. Nakamura, A. Nagai, K. Katayama, and K. Yamashita, "Dielectric properties of stoichiometric and defect-induced hydroxyapatite", *Journal of Applied Physics*, 113, (2013), 14935.

[75] A. Laghzizil, N. Elherch, A. Bouhaouss, G. Lorente, T. Coradin and J. Livage, "Electrical behavior of hydroxyapatites $M_{10}(PO_4)_6(OH)_2$ (M = Ca, Pb, Ba)", *Materials Research Bulletin* 36 (5-6), (2001), 953-962.

[76] B. Lu Hongbo, T. C. Charles, J. G. Daniel and D. R. Buddy, "Surface Characterization of Hydroxyapatite and Related Calcium Phosphates by XPS and TOF-SIMS", *Analytical Chemistry* 72(13), (2000), 2886-2894.

[77] H. Matsudo, K. Kakimoto and I. Kagomiya, "Thermal Depolarization measurement for $Na_{0.5}K_{0.5}NbO_3$piezoceramics", *Japanese Journal of Applied Physics* 49, (2010), 09MC07.

[78] K. Tanaka, S. Takatsuka, H. Nishiyama and K. Kakimoto, "Analyses of oxygen vacancies in (Na, K) NbO_3-series piezoelectric ceramics by soft x-ray emission spectroscopy", *AIP Advances* 9, (2019), 045102.

[79] Y. Huan, X. Wang, T. Wei, J. Xie, Z. Ye, P. Zhao and L. Li, "Defect engineering of high-performance potassium sodium niobate piezoelectric ceramics sintered in reducing atmosphere", *Journal of the American Ceramic Society*, 100, (2017), 2024-2033.

[80] A. Shigemi and T. Wada, "Enthalpy of Formation of Various Phases and Formation Energy of Point Defects in Perovskite-Type $NaNbO_3$ by First-Principles Calculation", *Japanese Journal of Applied Physics* 43, (2004), 6793-6798.

[81] A. Shigemi and T. Wada, "Evaluations of Phases and Vacancy Formation Energies in $KNbO_3$ by First-Principles Calculation", *Japanese Journal of Applied Physics* 44, (2005), 8048-8054.

[82] W. Liu and C. A. Randall, "Thermally Stimulated Relaxation in Fe-Doped $SrTiO_3$ Systems: II. Degradation of $SrTiO_3$ Dielectrics", *Journal of the American Ceramic Society*, 91, (2008), 3251-3257.

[83] W. Liu and C. A. Randall, "Thermally Stimulated Relaxation in Fe-Doped $SrTiO_3$ Systems: I. Single Crystals", *Journal of the American Ceramic Society* 91, (2008), 3245-3250.

[84] J.-F. Li, K. Wang and B.-P. Zhang and L.-M. Zhang, "Ferroelectric and Piezoelectric Properties of Fine-Grained $Na_{0.5}K_{0.5}NbO_3$ Lead-Free Piezoelectric Ceramics Prepared by Spark Plasma Sintering", *Journal of the American Ceramic Society* 89, (2006), 706-709.

[85] R. Pinho, A. Tkach, S. Zlotnik, M. E. Costa, J. Noudem, I. M. Reaney and P. M. Vilarinho, "Spark plasma texturing: A strategy to enhance the electro-mechanical properties of lead-free potassium sodium niobate ceramics", *Applied Materials Today*, 19, (2020), 100566.

[86] P. Li, X. Chen, F. Wang, B. Shen, J. Zhai, Z. Shujun Zhang and Z. Zhiyong, "Microscopic Insight into Electric Fatigue Resistance and Thermally Stable Piezoelectric Properties of $(K,Na)NbO_3$-Based Ceramics", *ACS Applied Materials and Interfaces* 10(34), (2018), 28772-28779.

[87] R. E. Jaeger and L. Egerton, "Hot pressing of potassium–sodium niobates", *Journal of the American Ceramic Society* 45(5), (1962), 209-213.

[88] X. Cheng, Q. Gou, J. Wu, X. Wang, B. Zhang, D. Xiao, J. Zhu, X. Wang and X. Lou, "Dielectric, ferroelectric, and piezoelectric properties in potassium sodium niobate ceramics with rhombohedral–orthorhombic and orthorhombic–tetragonal phase boundaries", *Ceramics International* 40(4), (2014), 5771-5779.

[89] M. A. Rafiq, M. E. Costa, A. Tkach and P.M. Vilarinho, "Impedance Analysis and Conduction Mechanism of Lead Free Potassium Sodium Niobate (KNN) single crystals and polycrystals: A Comparison study", *Crystal Growth and Design* 15(3), (2014), 1289-1294.

[90] S. Lanfredi, L. Dessemond and A.C. Rodrigues, "Effect of Porosity on the Electrical Properties of Polycrystalline Sodium Niobate: I, Electrical Conductivity", *Journal of the American Ceramic Society* 86, (2003), 291-298.

[91] R. Rani, S. Sharma, R. Rai and A.L. Kholkin, "Investgation of dielectric and electrical properties of Mn doped sodium potassium noiobate cramic system using impedance spectroscopy", *Journal of Applied Physics* 110, (2011), 104102.

[92] N. Horiuchi, Iwasaki, K. Nozaki, M. Nakamur, K. Hashimoto, A. Nagai and K. Yamashita, "A critical phenomenon of phase transition in hydroxyapatite investigated by thermally stimulated depolarization currents", *Journal of the American Ceramic Society*, 100, (2017), 501-505.

[93] E. M. Anton, W. Jo, D. Damjanovicand and J. Rödel, "Determination of depolarization temperature of $(Bi_1/2Na_{1/2})TiO_3$-based lead-free piezoceramics", *Journal of Applied Physics*, 119, (9), (2011), 094108.

[94] F. Guo, B. Yang, Bin, S. Zhang, F. Wu, D. Liu, P. Hu, Y. Sun, D. Wang and W. Cao, "Enhanced pyroelectric property in $(1-x)(Bi_{0.5}Na_{0.5})TiO_3$-$xBa(Zr_{0.055}Ti_{0.945})O_3$: Role of morphotropic phase boundary and ferroelectric-antiferroelectric phase transition", *Applied Physics Letters*, 103(18), (2013), 182906.

[95] T. N. M. Ngo, U. Adem and T. T. M. Palstra, "The origin of thermally stimulated depolarization currents in multiferroic $CuCrO_2$", *Applied Physics Letters*, 106(15), (2015), 152904.

[96] A.S. Verma, A. Sharma, A. Kumar, A. Mukhopadhyay, D. Kumar, and A. K. Dubey, "Multifunctional Response of Piezoelectric Sodium Potassium Niobate (NKN)-Toughened Hydroxyapatite-Based Biocomposites", *ACS Applied Bio Materials* 3 (8), (2020), 5287-5299.

[97] A. K. Dubey and K. Kakimoto, "Impedance spectroscopy and mechanical response of porous nanophase hydroxyapatite–barium titanate composite", *Materials Science and Engineering: C*, 63, (2016), 211-221.